von Karman Institute for Fluid Dynamics

Lecture Series 1999-03

30^{TH} COMPUTATIONAL FLUID DYNAMICS

March 8 - 12, 1999

LOW MACH NUMBER ASYMPTOTICS OF THE NAVIER-STOKES EQUATIONS AND NUMERICAL IMPLICATIONS

B. Müller
Uppsala University, Sweden

Low Mach Number Asymptotics of the Navier-Stokes Equations and Numerical Implications

B. Müller
Department of Scientific Computing, Information Technology, Uppsala University, P.O. Box 120, S-751 04 Uppsala, Sweden

Abstract

Low Mach number asymptotics of the Navier-Stokes equations reveals the role of the large global thermodynamic pressure, the small acoustic pressure and the very small 'incompressible' pressure. Solving for the changes of the conservative variables with respect to stagnation conditions retains the conservative discretization and avoids the cancellation problem, when computing the small changes in low Mach number flow.

Key words: Navier-Stokes equations, asymptotic analysis, low Mach number flow, aeroacoustics, cancellation, perturbation formulation, finite volume method, approximate Riemann solver.

Notation: In this lecture, all physical quantities with superscript * are dimensional and all physical quantities without superscript * are nondimensional. Unless stated otherwise, the nondimensionalization (13) is used.

Introduction

Speaking, singing and playing a music instrument are pleasant examples of compressible low Mach number flow, unless they are considered as noise. Acoustics in gases and liquids is not only a daily experience, but also has great scientific and technological significance. Aerodynamic noise regulations have become more restrictive due to public demands caused by increased transport of persons and goods and by increased environmental sensitivity. Thus, aeroacoustics has become a key issue in the design of airplanes, helicopters, trains, cars, engines, gas turbines, etc. The available computational power and emerging numerical methods have recently led to computational aeroacoustics (CAA) as a new branch of computational fluid dynamics (CFD). Like CFD, CAA offers great potential to complement theoretical and experimental aeroacoustic research. Therefore, Sir James Lighthill foresees a "second golden age of aeroacoustics" [1].

Since in many practical applications the sound generation is primarily determined by the slow vorticity fluctuations in a turbulent flow, there has been considerable interest in low Mach number computational aeroacoustics. Crighton argues [2]:
"First, why is there interest in low Mach number aeroacoustics at all, whether analytical,

experimental or computational?
...; unless the mean flow exceeds roughly *twice* the ambient speed of sound (...) the radiation is determined primarily by the slow temporal evolution of convected eddies; ...
Second, why are we making a fuss about *computational* aeroacoustics?
... The problem is that *all numerical analysis procedures are inherently noisy* (in the acoustic sense). ... the numerical procedure may actually be "noisier" than the flow! ...
In aeroacoustics we are dealing with the *minutest* energy levels, compared with the whole flow - and moreover, with those energies on length scales $O(M^{-1})$ larger than the scales of the "energy-containing eddies". Calculations of these lie, in energy and scale, far outside the range of conditions adequately resolved by standard CFD procedures. This is what makes *computational aeroacoustics* at low Mach number not merely a *technologically*, but also a *scientifically*, important problem."

However, it is not only aeroacoustics, which makes compressible low Mach number flow such an interesting problem. Even in hypersonic flow, there are low Mach number regions in the vicinity of stagnation points and no-slip surfaces, at which the velocity is zero. Separated flow is often characterized by low Mach numbers. Whereas conventional compressible flow codes perform rather well for transonic flow, their accuracy and efficiency deteriorates considerably as the Mach number approaches zero [3]. Therefore, the computation of compressible low Mach number flow is an important issue in CFD both for steady and unsteady flow.

In the first part of this lecture, low Mach number asymptotic analyses are performed to get better mathematical insight into the Navier-Stokes equations and better physical understanding of the mechanisms they describe, as the Mach number M goes to zero.

In the second part of this lecture, numerical implications are drawn from the asymptotic analyses and from physical facts in low Mach number flow. The cancellation problem and its solution by the perturbation form of the Navier-Stokes equations are described in detail.

The conclusions are stated in the third part.

1 Low Mach Number Asymptotics of the Navier-Stokes Equations

1.1 Review and Outline

Low Mach number asymptotics is used by Klainerman and Majda [4] for the Euler equations and by Kreiss et al. [5] for the Navier-Stokes equations to prove the convergence of the compressible flow solutions to the incompressible flow solutions for $M \to 0$ under certain conditions. Majda [6] employs low Mach number asymptotics to derive the equations for low Mach number combustion. The resonant interaction of small amplitude periodic high frequency acoustic waves with entropy and vorticity waves is studied by Hunter et al. [7], Majda et al. [8], Almgren [9] and other authors using the method of multiple scales. Rehm and Baum [10] derive the low Mach number limit of the compressible Euler equations for buoyant inviscid flow with heat release. For the low Mach number limit of the compressible Navier-Stokes equations, Fedorchenko [11] provides a number of exact solutions. Employing multiple time and space scale expansions, Zank and Matthaeus [12] derive low Mach number equations from the compressible Navier-Stokes equations. The single time scale, multiple space scale asymptotic analysis by Klein [13] yields insight into the low Mach number limit behaviour of the compressible Euler equations and has been

used to develop a numerical method for low Mach number flow with long wave acoustics. While Klein [13] considers inviscid low Mach number flow with small spatial flow scales and large spatial acoustic scales for the same flow time scale, Müller investigates [14], [15] the low Mach number behavior of viscous flow with small acoustic and large flow time scales for the same geometric space scale. The zero Mach number limit of the multiple time scale, single space scale asymptotic analysis is related to the low Mach number equations [14], [15]. For small turbulent Mach numbers, a single space scale, multiple time scale asymptotics allows Ristorcelli [16] to distinguish advective and acoustic modes in a vortical source of sound and to find a closure for the compressible aspects of the source terms in Lighthill's acoustic analogy.

The objective of this first part of the lecture is to give insight into the low Mach number limit of the Navier-Stokes equations by means of asymptotic analysis. After stating the Navier-Stokes equations for compressible flow in section 1.2, they are nondimensionalized in section 1.3. In section 1.4, we demonstrate low Mach number asymptotics and derive the low Mach number Navier-Stokes equations by the single time scale and single space scale asymptotic analysis following Rehm and Baum [10] and Majda [6], [17]. The low Mach number equations are related to the Boussinesq and incompressible flow equations. The multiple time scale and single space scale asymptotic analysis of the Navier-Stokes equations by Müller [14], [15] is presented in section 1.5. Contrary to the low Mach number equations, acoustic effects are taken into account. In section 1.6, the acoustic waves are explicitly removed by averaging over a short acoustic time period. If even the net effect of acoustics is neglected, we again obtain the low Mach number equations. Finally, the roles of the pressure in low Mach number flow are discussed.

1.2 Navier-Stokes Equations

The conservation laws of mass, momentum and energy for a compressible viscous fluid flow are called the Navier-Stokes equations in computational fluid dynamics. They read in differential conservative form:

continuity equation

$$\frac{\partial \rho^*}{\partial t^*} + \boldsymbol{\nabla}^* \cdot (\rho^* \mathbf{u}^*) = 0, \tag{1}$$

momentum equation

$$\frac{\partial \rho^* \mathbf{u}^*}{\partial t^*} + \boldsymbol{\nabla}^* \cdot (\rho^* \mathbf{u}^* \mathbf{u}^*) + \boldsymbol{\nabla}^* p^* = \mathbf{G}^*, \tag{2}$$

energy equation

$$\frac{\partial \rho^* E^*}{\partial t^*} + \boldsymbol{\nabla}^* \cdot (\rho^* H^* \mathbf{u}^*) = Q^*. \tag{3}$$

All dimensional quantities are denoted by superscript *, e.g. time t^*. ρ^*, p^*, $\mathbf{u}^*$ denote the density, pressure and velocity vector, respectively. The vector operators $\boldsymbol{\nabla}^* \cdot$ and $\boldsymbol{\nabla}^*$ are the divergence and gradient, respectively. In Cartesian coordinates, the components of the postion vector, velocity vector and nabla operator are given by $\mathbf{x}^* = (x^*, y^*, z^*)^T$, $\mathbf{u}^* = (u^*, v^*, w^*)^T$ and $\boldsymbol{\nabla}^* = (\frac{\partial}{\partial x^*}, \frac{\partial}{\partial y^*}, \frac{\partial}{\partial z^*})^T$, respectively.

$\mathbf{G}^*$ represents the sum of external forces. Here we consider viscous and buoyancy forces

$$\mathbf{G}^* = \boldsymbol{\nabla}^* \cdot \boldsymbol{\tau}^* + \rho^* \mathbf{g}^*. \tag{4}$$

For a Newtonian fluid, the shear stress tensor $\boldsymbol{\tau}^*$ is given by

$$\boldsymbol{\tau}^* = \mu^* (\boldsymbol{\nabla}^* \mathbf{u}^* + (\boldsymbol{\nabla}^* \mathbf{u}^*)^T) - \frac{2}{3} \mu^* \boldsymbol{\nabla}^* \cdot \mathbf{u}^* \, \mathbf{I} \tag{5}$$

with the (dynamic) viscosity μ^*, which depends on temperature T^*. $\mathbf{I}$ is the unit tensor. The gravitational acceleration vector $\mathbf{g}^*$ is directed opposite to the radial unit vector $\mathbf{e}_r$ in spherical coordinates with the gravity constant $g^* = 9.81 \frac{m}{s^2}$ on the earth surface:

$$\mathbf{g}^* = -g^* \mathbf{e}_r. \tag{6}$$

$$E^* = e^* + \frac{1}{2} |\mathbf{u}^*|^2 \tag{7}$$

denotes the total energy per unit mass, i.e. the sum of internal energy e^* and kinetic energy $\frac{1}{2}|\mathbf{u}^*|^2$.

$$H^* = E^* + \frac{p^*}{\rho^*} \tag{8}$$

is the total enthalpy.

Q^* is the sum of the work done by the external forces, the energy input by heat conduction and the heat released by external sources per unit volume and per unit time, i.e.

$$Q^* = \boldsymbol{\nabla}^* \cdot (\boldsymbol{\tau}^* \cdot \mathbf{u}^*) + \rho^* \mathbf{g}^* \cdot \mathbf{u}^* + \boldsymbol{\nabla}^* \cdot (\kappa^* \boldsymbol{\nabla}^* T^*) + \rho^* q^* \tag{9}$$

The Fourier law is assumed for the heat conduction term, in which the heat conduction coefficient κ^* depends on temperature T^*. The heat release rate q^* might be due to chemical reactions.

If viscosity and heat conduction are negligible, i.e. $\mu^* \equiv 0$ and $\kappa^* \equiv 0$, the Euler equations are obtained. Thereby, the type of the equations is changed from hyperbolic-parabolic to hyperbolic [18].

If buoyancy is negligible, i.e. $g^* \equiv 0$, $\mathbf{G}^*$ and Q^* are simplified.

For a perfect gas, the thermodynamic quantities are related by the equations of state

$$p^* = \rho^* R^* T^*, \tag{10}$$

$$e^* = c_v^* T^* \tag{11}$$

with the specific gas constant $R^* = c_p^* - c_v^*$ and the specific heats at constant pressure and volume c_p^* and c_v^*, respectively. The ratio of specific heats is

$$\gamma = \frac{c_p^*}{c_v^*}. \tag{12}$$

For air at standard conditions, $\gamma = 1.4$.

1.3 Nondimensionalization

The equations (1) to (11) are nondimensionalized by using reference quantities denoted by the subscript ∞, e.g. farfield or stagnation conditions, and a typical length scale L^* of the considered flow. The thermodynamic reference quantities are assumed to be related by the equation of state (10) for perfect gas. We define the nondimensional quantities by:

$$\begin{aligned} \rho &= \frac{\rho^*}{\rho^*_\infty}, \quad p = \frac{p^*}{p^*_\infty}, \quad \mathbf{u} = \frac{\mathbf{u}^*}{u^*_\infty}, \quad T = \frac{T^*}{T^*_\infty}, \quad \mu = \frac{\mu^*}{\mu^*_\infty}, \quad \kappa = \frac{\kappa^*}{\kappa^*_\infty}, \\ \mathbf{x} &= \frac{\mathbf{x}^*}{L^*}, \quad t = \frac{t^*}{L^*/u^*_\infty}, \\ e &= \frac{e^*}{p^*_\infty/\rho^*_\infty}, \quad E = \frac{E^*}{p^*_\infty/\rho^*_\infty}, \quad H = \frac{H^*}{p^*_\infty/\rho^*_\infty}. \end{aligned} \tag{13}$$

The reference quantities are chosen such that the nondimensional flow quantities remain of order O(1) for any low reference Mach number

$$M_\infty = \frac{u^*_\infty}{\sqrt{\gamma p^*_\infty/\rho^*_\infty}}. \tag{14}$$

To avoid the dependence on γ, we shall work with:

$$\tilde{M} = \frac{u^*_\infty}{\sqrt{p^*_\infty/\rho^*_\infty}} = \sqrt{\gamma} M_\infty. \tag{15}$$

Note that with other nondimensionalizations

$$\begin{aligned} \tfrac{u^*}{\sqrt{p^*_\infty/\rho^*_\infty}} &= \tfrac{u^*}{u^*_\infty}\tilde{M} \to 0 \text{ for } \tilde{M} \to 0, \text{ and} \\ \tfrac{p^*}{\rho^*_\infty u^{*2}_\infty} &= \tfrac{p^*}{p^*_\infty}\tfrac{1}{\tilde{M}^2} \to \infty \text{ for } \tilde{M} \to 0. \end{aligned}$$

Using the relations (13) in the equations of section 1.2, the nondimensional Navier-Stokes equations read:

$$\frac{\partial \rho}{\partial t} + \boldsymbol{\nabla} \cdot (\rho \mathbf{u}) = 0, \tag{16}$$

$$\frac{\partial \rho \mathbf{u}}{\partial t} + \boldsymbol{\nabla} \cdot (\rho \mathbf{u}\mathbf{u}) + \frac{1}{\tilde{M}^2}\boldsymbol{\nabla} p = \mathbf{G}, \tag{17}$$

$$\frac{\partial \rho E}{\partial t} + \boldsymbol{\nabla} \cdot (\rho H \mathbf{u}) = Q. \tag{18}$$

The right hand side of the nondimensional momentum equation (17) reads

$$\mathbf{G} = \frac{1}{Re_\infty}\boldsymbol{\nabla} \cdot \boldsymbol{\tau} + \frac{1}{Fr^2_\infty}\rho(-\mathbf{e}_r) \tag{19}$$

with $Re_\infty = \frac{\rho^*_\infty u^*_\infty L^*}{\mu^*_\infty}$ the Reynolds number, $Fr_\infty = \frac{u^*_\infty}{\sqrt{g^* L^*}}$ the Froude number and $\boldsymbol{\tau} = \mu(\boldsymbol{\nabla}\mathbf{u} + (\boldsymbol{\nabla}\mathbf{u})^T) - \frac{2}{3}\mu \boldsymbol{\nabla} \cdot \mathbf{u}\, \mathbf{I}$ the nondimensional shear stress tensor.

The right hand side of the nondimensional energy equation (18) reads

$$Q = \frac{\tilde{M}^2}{Re_\infty}\boldsymbol{\nabla}\cdot(\boldsymbol{\tau}\cdot\mathbf{u}) + \frac{\tilde{M}^2}{Fr_\infty^2}\rho(-\mathbf{e}_r)\cdot\mathbf{u} + \frac{\gamma}{(\gamma-1)Re_\infty Pr_\infty}\boldsymbol{\nabla}\cdot(\kappa\boldsymbol{\nabla}T) + \rho q \tag{20}$$

with $Pr_\infty = \frac{c_p^*\mu_\infty^*}{\kappa_\infty^*}$ the Prandtl number
and $q = \frac{q^*}{\frac{u_\infty^* p_\infty^*}{L^*\rho_\infty^*}}$ the nondimensional heat release rate.

The nondimensional expressions of the total energy per unit mass and the total enthalpy are

$$E = e + \tilde{M}^2\frac{1}{2}|\mathbf{u}|^2, \tag{21}$$

$$H = E + \frac{p}{\rho}. \tag{22}$$

The nondimensional equations of state for a perfect gas read

$$p = \rho T, \tag{23}$$

$$e = \frac{1}{\gamma-1}T. \tag{24}$$

Using equations (23), (24) and (21), the pressure can be expressed in terms of the conservative variables ρ, $\rho\mathbf{u}$ and ρE by

$$p = (\gamma-1)[\rho E - \tilde{M}^2\frac{1}{2}\frac{|\rho\mathbf{u}|^2}{\rho}]. \tag{25}$$

If we assume $Pr = \frac{c_p^*\mu^*}{\kappa^*} = Pr_\infty$ and $c_p^* = \text{const}$, we obtain $\frac{\kappa^*}{\kappa_\infty^*} = \frac{\mu^*}{\mu_\infty^*}$. Then:

$$\kappa = \mu. \tag{26}$$

The viscosity might for example be determined by the Sutherland law

$$\mu = T^{\frac{3}{2}}\frac{1+S}{T+S} \tag{27}$$

with $S = \frac{110K}{T_\infty^*}$ for air at standard conditions.

1.4 Single Scale Asymptotic Analysis

Before addressing the numerical solution of the Navier-Stokes equations in part 2, we shall employ perturbation methods [19], [20] to derive approximations of the Navier-Stokes equations at low Mach numbers and to get insight into the underlying physical mechanisms. The asymptotic analysis allows to identify terms that can be neglected, as a parameter - in our case the reference Mach number or $\tilde{M}$ - becomes small. Here, we illustrate the regular perturbation method by deriving the low Mach number equations. We follow the asymptotic analysis by Rehm and Baum [10] for inviscid thermally driven buoyant flow and by Majda [6], [17] for low Mach number combustion.

We assume that the independent variables are fully characterized by the length scale L^* and the time scale L^*/u_∞^* used to nondimensionalize the space and time variables $\mathbf{x}^*$ and t^* in (13). Thus, we assume that the single time scale variable t and the single space

scale variable $\mathbf{x}$ fully describe the low Mach number flow. Moreover, we assume that the low Mach number asymptotic analysis is a regular perturbation problem, i.e. all flow variables can be expanded in power series of $\tilde{M}$ as for example the pressure

$$p(\mathbf{x}, t, \tilde{M}) = p_0(\mathbf{x}, t) + \tilde{M} p_1(\mathbf{x}, t) + \tilde{M}^2 p_2(\mathbf{x}, t) + O(\tilde{M}^3). \tag{28}$$

p_0, p_1 and p_2 are called the zeroth- (or leading), first- and second-order pressure, respectively.

Inserting the asymptotic expansions of $\rho\mathbf{u}$, ρ and $\mathbf{u}$ into the definition of the momentum density as density times velocity

$$\rho\mathbf{u} \;=\; \rho\,\mathbf{u}, \tag{29}$$

yields

$$\begin{aligned} & (\rho\mathbf{u})_0 + \tilde{M}(\rho\mathbf{u})_1 + \tilde{M}^2(\rho\mathbf{u})_2 + O(\tilde{M}^3) \\ = \;& (\rho_0 + \tilde{M}\rho_1 + \tilde{M}^2\rho_2 + O(\tilde{M}^3))\,(\mathbf{u}_0 + \tilde{M}\mathbf{u}_1 + \tilde{M}^2\mathbf{u}_2 + O(\tilde{M}^3)) \\ = \;& \rho_0\mathbf{u}_0 + \tilde{M}(\rho_0\mathbf{u}_1 + \rho_1\mathbf{u}_0) + \tilde{M}^2(\rho_0\mathbf{u}_2 + \rho_1\mathbf{u}_1 + \rho_2\mathbf{u}_0) + O(\tilde{M}^3). \end{aligned} \tag{30}$$

Ordering the terms in equation (30) according to the powers of $\tilde{M}$ leads to the equation

$$[(\rho\mathbf{u})_0 - \rho_0\mathbf{u}_0] + [(\rho\mathbf{u})_1 - (\rho_0\mathbf{u}_1 + \rho_1\mathbf{u}_0)]\tilde{M} + [(\rho\mathbf{u})_2 - (\rho_0\mathbf{u}_2 + \rho_1\mathbf{u}_1 + \rho_2\mathbf{u}_0)]\tilde{M}^2 + O(\tilde{M}^3) \;=\; 0. \tag{31}$$

Since equation (31) is supposed to hold for arbitrary values of $\tilde{M}$, the coefficients of the monomials $\tilde{M}^l, l = 0, 1, 2, ...$, must be zero. Therefore, we obtain for the zeroth-, first- and second-order momentum densities

$$(\rho\mathbf{u})_0 \;=\; \rho_0\mathbf{u}_0, \tag{32}$$

$$(\rho\mathbf{u})_1 \;=\; \rho_0\mathbf{u}_1 + \rho_1\mathbf{u}_0, \tag{33}$$

$$(\rho\mathbf{u})_2 \;=\; \rho_0\mathbf{u}_2 + \rho_1\mathbf{u}_1 + \rho_2\mathbf{u}_0. \tag{34}$$

Thus, we can express the zeroth-, first- and second-order velocities as

$$\mathbf{u}_0 \;=\; (\rho\mathbf{u})_0/\rho_0, \tag{35}$$

$$\mathbf{u}_1 \;=\; ((\rho\mathbf{u})_1 - \rho_1\mathbf{u}_0)/\rho_0, \tag{36}$$

$$\mathbf{u}_2 \;=\; ((\rho\mathbf{u})_2 - \rho_1\mathbf{u}_1 - \rho_2\mathbf{u}_0)/\rho_0. \tag{37}$$

Similarly, we use the relation (25) and the nondimensional equation of state (23) to express the pressure and thereby also the temperature in terms of the conservative variables. The asymptotic expansion yields

$$p_0 = (\gamma - 1)(\rho E)_0, \tag{38}$$

$$p_1 = (\gamma - 1)(\rho E)_1, \tag{39}$$

$$p_2 = (\gamma - 1)[(\rho E)_2 - \frac{1}{2}\rho_0|\mathbf{u}_0|^2], \tag{40}$$

$$T_0 = \frac{p_0}{\rho_0}, \tag{41}$$

$$T_1 = \frac{p_1 - \rho_1 T_0}{\rho_0}, \tag{42}$$

$$T_2 = \frac{p_2 - \rho_1 T_1 - \rho_2 T_0}{\rho_0}. \tag{43}$$

Using the definition of the total enthalpy (22) and the equations (38) and (39), the asymptotic expansion yields

$$(\rho H)_0 = \frac{\gamma}{\gamma - 1} p_0 \tag{44}$$

and

$$(\rho H)_1 = \frac{\gamma}{\gamma - 1} p_1. \tag{45}$$

The asymptotic expansion of $\rho H \mathbf{u}$ equal ρH times $\mathbf{u}$ yields

$$(\rho H \mathbf{u})_0 = (\rho H)_0 \mathbf{u}_0, \tag{46}$$

$$(\rho H \mathbf{u})_1 = (\rho H)_0 \mathbf{u}_1 + (\rho H)_1 \mathbf{u}_0. \tag{47}$$

After the asymptotic analysis of the algebraic equations, we shall now consider the partial differential equations. Inserting the asymptotic expansions of the density ρ and the momentum density $\rho\mathbf{u}$ into the continuity equation (16) and ordering according to powers of $\tilde{M}$ leads to

$$[\frac{\partial \rho_0}{\partial t} + \boldsymbol{\nabla} \cdot (\rho \mathbf{u})_0] + [\frac{\partial \rho_1}{\partial t} + \boldsymbol{\nabla} \cdot (\rho \mathbf{u})_1]\tilde{M} + [\frac{\partial \rho_2}{\partial t} + \boldsymbol{\nabla} \cdot (\rho \mathbf{u})_2]\tilde{M}^2 + O(\tilde{M}^3) \;=\; 0. \tag{48}$$

Requiring the coefficients of $\tilde{M}^l, l = 0, 1, 2$, i.e. the terms in square brackets in (48), to vanish we obtain

$$\frac{\partial \rho_l}{\partial t} + \boldsymbol{\nabla} \cdot (\rho \mathbf{u})_l \;=\; 0, \qquad l = 0, 1, 2. \tag{49}$$

For the momentum equation (17), we obtain after inserting the asymptotic expansions of all flow variables involved and ordering according to the powers of $\tilde{M}$

$$\boldsymbol{\nabla} p_0 \tilde{M}^{-2} + \boldsymbol{\nabla} p_1 \tilde{M}^{-1} + \frac{\partial \rho_0 \mathbf{u}_0}{\partial t} + \boldsymbol{\nabla} \cdot (\rho_0 \mathbf{u_0} \mathbf{u_0}) + \boldsymbol{\nabla} p_2 - \mathbf{G}_0 + O(\tilde{M}) \;=\; 0, \tag{50}$$

where $\mathbf{G}_0 = \frac{1}{Re_\infty} \boldsymbol{\nabla} \cdot \boldsymbol{\tau}_0 + \frac{1}{Fr_\infty^2} \rho_0 (-\mathbf{e}_r)$ with $\boldsymbol{\tau}_0 = \mu_0 (\boldsymbol{\nabla} \mathbf{u}_0 + (\boldsymbol{\nabla} \mathbf{u}_0)^T) - \frac{2}{3} \mu_0 \boldsymbol{\nabla} \cdot \mathbf{u}_0 \, \mathbf{I}$.
We assume that the Reynolds and Froude numbers are fixed as we vary the Mach number. In equation (50), we require the coefficients of $\tilde{M}^l, l = -2, -1, 0$, to vanish. Thus, we get the relations

$$\boldsymbol{\nabla} p_0 \;=\; 0, \tag{51}$$

$$\boldsymbol{\nabla} p_1 \;=\; 0, \tag{52}$$

$$\frac{\partial \rho_0 \mathbf{u}_0}{\partial t} + \boldsymbol{\nabla} \cdot (\rho_0 \mathbf{u_0} \mathbf{u_0}) + \boldsymbol{\nabla} p_2 \;=\; \mathbf{G}_0. \tag{53}$$

For the energy equation, we proceed similarly as for the continuity equation and obtain

$$\frac{\partial (\rho E)_l}{\partial t} + \boldsymbol{\nabla} \cdot (\rho H \mathbf{u})_l \;=\; Q_l, \qquad l = 0, 1, 2, \tag{54}$$

where $Q_l = \frac{\gamma}{(\gamma - 1) Re_\infty Pr_\infty} \boldsymbol{\nabla} \cdot (\kappa \boldsymbol{\nabla} T)_l + (\rho q)_l, \quad l = 0, 1,$
and $Q_2 = \frac{1}{Re_\infty} \boldsymbol{\nabla} \cdot (\boldsymbol{\tau}_0 \cdot \mathbf{u}_0) + \frac{1}{Fr_\infty^2} \rho_0 (-\mathbf{e}_r) \cdot \mathbf{u}_0 + \frac{\gamma}{(\gamma - 1) Re_\infty Pr_\infty} \boldsymbol{\nabla} \cdot (\kappa \boldsymbol{\nabla} T)_2 + (\rho q)_2$.
Equations (51) and (52) derived from the asymptotic analysis of the momentum equation imply that

$$p_0 \;=\; p_0(t) \tag{55}$$

and

$$p_1 \;=\; p_1(t), \tag{56}$$

i.e. p_0 and p_1 are functions of time only. Using equations (38) and (39), we arrive at a similar conclusion for the zeroth- and first-order total energy densities, i.e.

$$(\rho E)_0 \;=\; (\rho E)_0(t) \tag{57}$$

and

$$(\rho E)_1 \;=\; (\rho E)_1(t). \tag{58}$$

Inserting equations (38), (46), (44) and (39), (47), (45) into the zeroth- and first-order energy equations (54) for $l = 0$ and $l = 1$, respectively, we obtain

$$\frac{dp_0}{dt} + \gamma p_0 \boldsymbol{\nabla} \cdot \mathbf{u}_0 \;=\; (\gamma - 1) Q_0 \tag{59}$$

and

$$\frac{dp_1}{dt} + \gamma p_0 \boldsymbol{\nabla} \cdot \mathbf{u}_1 + \gamma p_1 \boldsymbol{\nabla} \cdot \mathbf{u}_0 \;=\; (\gamma - 1) Q_1. \tag{60}$$

Using the zeroth-order continuity equation (49), $l = 0$, and the zeroth-order equation of state (41), the zeroth-order energy equation (54), $l = 0$, can be expressed as

$$\frac{\gamma}{\gamma - 1} \rho_0 [\frac{\partial T_0}{\partial t} + \mathbf{u}_0 \cdot \boldsymbol{\nabla} T_0] - \frac{dp_0}{dt} = Q_0. \tag{61}$$

Multiplying the first-order Navier-Stokes equations (49), (52), (54), $l = 1$, by $\tilde{M}$ and adding the zeroth-order Navier-Stokes equations (49), (51), (54), $l = 0$, we obtain the same equations for

$$\tilde{\mathbf{V}}_0 \;=\; \mathbf{V}_0 + \tilde{M} \mathbf{V}_1 \tag{62}$$

as the zeroth-order Navier-Stokes equations for $\mathbf{V}_0$, where $\mathbf{V} = (\rho, \mathbf{u}, p)^T$. Thus, we do not win any new information by the first-order expansion $\mathbf{V}_1$, and we can equally well start off the asymptotic analysis by expansions of the form

$$p(\mathbf{x}, t, \tilde{M}) = p_0(\mathbf{x}, t) + \tilde{M}^2 p_2(\mathbf{x}, t) + O(\tilde{M}^3) \tag{63}$$

instead of (28).

Let us summarize the single scale asymptotic analysis: If a space scale L^* and the time scale L^*/u^*_∞, i.e. the time it takes the reference flow to traverse the distance L^*, fully describe the considered low Mach number flow, the low Mach number limit yields the zeroth-order Navier-Stokes equations (49), $l = 0$, (53), (61), i.e.

$$\frac{\partial \rho_0}{\partial t} + \boldsymbol{\nabla} \cdot (\rho \mathbf{u})_0 \;=\; 0, \tag{64}$$

$$\frac{\partial \rho_0 \mathbf{u}_0}{\partial t} + \boldsymbol{\nabla} \cdot (\rho_0 \mathbf{u_0} \mathbf{u_0}) + \boldsymbol{\nabla} p_2 \;=\; \mathbf{G}_0. \tag{65}$$

$$\frac{\gamma}{\gamma - 1} \rho_0 [\frac{\partial T_0}{\partial t} + \mathbf{u}_0 \cdot \boldsymbol{\nabla} T_0] - \frac{dp_0}{dt} = Q_0. \tag{66}$$

With (55), the zeroth-order equation of state (41) reads

$$p_0(t) \;=\; \rho_0(\mathbf{x}, t) T_0(\mathbf{x}, t). \tag{67}$$

The zeroth-order Navier-Stokes equations (64), (65), (66), (67) are called low Mach number equations or zero Mach number equations. For combustion, the heat release rate $(\rho q)_0$ depends on chemical reactions and therefore on the involved species densities, which are determined by the species continuity equations [17], [21].

The zeroth-order pressure p_0 can be determined by integrating the zeroth-order energy equation in the form (59) over the volume V of the computational domain [10]

$$\frac{dp_0}{dt}\int_V dV + \gamma p_0 \int_{\partial V} \mathbf{u}_0 \cdot \mathbf{n}\, dA = (\gamma - 1)\int_V Q_0\, dV \tag{68}$$

Knowing the volume flow $\int_{\partial V} \mathbf{u}_0 \cdot \mathbf{n} dA$ and the total heat conduction and heat release rate $\int_V Q_0 dV$ in the computational domain, the ODE (68) can be solved for $p_0(t)$ starting from an initial condition $p_0(0)$.

The energy equation (66) is an evolution equation for the temperature $T_0(\mathbf{x}, t)$. The density $\rho_0(\mathbf{x}, t)$ is determined by the equation of state (67). The energy equation in the form (59) implies for the divergence of the velocity

$$\boldsymbol{\nabla} \cdot \mathbf{u}_0 \;=\; \frac{\gamma - 1}{\gamma p_0} Q_0 - \frac{1}{\gamma p_0}\frac{dp_0}{dt}. \tag{69}$$

Thus, the divergence of $\mathbf{u}_0$ is affected by the heat conduction and heat release rate Q_0 and the time change of the zeroth-order pressure p_0. Although the divergence of $\mathbf{u}_0$ is in general not zero, the roles of the velocity $\mathbf{u}_0$ and the second-order pressure p_2 are similar to velocity and pressure in incompressible flow. Assuming the density ρ_0 and the right hand side of equation (69), i.e. γ, p_0, $\frac{dp_0}{dt}$ and Q_0, to be known, we may determine $\mathbf{u}_0$ and p_2 similarly as in incompressible flow. For any smooth $\mathbf{u}_0$ and ρ_0, the divergence of the momentum equation (65) yields a Poisson equation for the second-order pressure p_2. At this point, the viscous and buoyancy forces described by $\mathbf{G}_0$ come into play. $\mathbf{u}_0$ is determined by the divergence constraint (69).

Of course, the density ρ_0 couples the momentum and energy equations via the equation of state (67). That coupling is more involved than the coupling via the buoyancy term in the Boussinesq equations, which are only valid for small density and temperature variations [10]. To the contrary, the low Mach number equations (64), (65), (66), (67) admit large density and temperature variations. For small density and temperature variations, the Boussinesq equations can be derived from the low Mach number equations [10]. If buoyancy in the Boussinesq equations can be neglected, the energy equation is decoupled from the momentum and continuity equations, which become the incompressible flow equations [10].

The second-order pressure p_2 in the low Mach number equations has an important property in common with the pressure in the Boussinesq equations and in the incompressible Euler and Navier-Stokes equations: The pressure is decoupled from density and temperature fluctuations arising through the equation of state. Instead, the pressure is determined by the constraint on the divergence of velocity. Therefore, acoustic waves are removed from the low Mach number equations like from the Boussinesq and incompressible flow equations. Consequently, similar methods as for the Boussinesq and incompressible flow equations can be used to solve the low Mach number equations numerically, e.g [17], [21].

1.5 Multiple Scales Asymptotic Analysis

The objective of this section is to give insight into the compressible Navier-Stokes equations at low Mach number, when slow flow is affected by acoustic effects in a bounded

region over a long time. We may think of a modern gas turbine combustor, where acoustic waves are reflected at the turbine inlet and the upstream wall and interact many times with the turbulent flame [22].

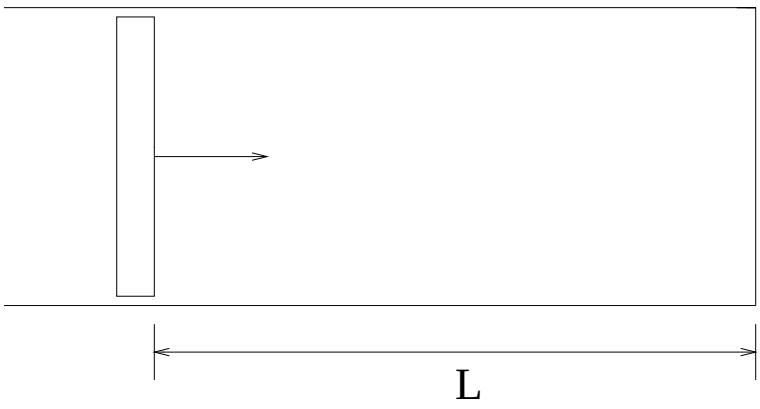

Figure 1: Piston slowly moving in a cylinder.

Another application in mind is a closed piston-cylinder system (Fig. 1), in which the isentropic compression due to a slow piston motion is modified by acoustic waves. These are generated by the piston start and propagate back and forth many times, because they are reflected at the cylinder end and piston. In that problem, we have one length scale, say the initial distance between piston and cylinder end, and two time scales: the long time it takes the slow flow, i.e. the piston, to travel one length scale and the short time it takes an acoustic wave to travel one length scale. Opposed to a regular low Mach number expansion, an asymtotic analysis with two time scales and one space scale together with the analytical method of characteristics avoids secular (i.e. singular) terms and allows G.H. Schneider [23] (cf. W. Schneider [19], pp. 235-240) and Klein and Peters [24] to account for the cumulative acoustic effects in the inert and reacting piston-cylinder problems, respectively. Using a similar asymptotic approach, Rhadwan and Kassoy [25] investigate the acoustic response due to boundary heating in a confined inert gas. Here, the multiple time scale and single space scale asymptotic analysis is employed to get a better understanding of the low Mach number limit of the compressible Navier-Stokes equations and to derive simplified equations, which account for the net effect of periodic acoustic waves on slow flow over a long time. The present work is based on the author's habilitation thesis [14] and the article [15]. A general description of multiple scales asymptotic analysis may be found in [19], [26].

Since we are interested in slow flow affected by acoustic effects in a confined gas over a long time, we introduce the fast acoustic time scale

$$\tau_\infty^* = \frac{L^*}{\sqrt{\frac{p_\infty^*}{\rho_\infty^*}}}. \tag{70}$$

The acoustic time scale variable is defined by

$$\tau = \frac{t^*}{\tau_\infty^*} = \frac{t}{\tilde{M}} \tag{71}$$

The flow and acoustic time scales are illustrated in Figs. 2 and 3 for the two characteristics $\frac{dx^*}{dt^*} = u_\infty^*$ and $\frac{dx^*}{dt^*} = \sqrt{\frac{p_\infty^*}{\rho_\infty^*}} = \frac{c_\infty^*}{\sqrt{\gamma}}$, respectively. Whereas the flow time scale is determined

by the time it takes the reference flow to travel one length scale, the acoustic time scale corresponds to the time it takes to travel one length scale at the reference speed of sound divided by $\sqrt{\gamma}$. In the two time scale, single space scale low Mach number asymptotic

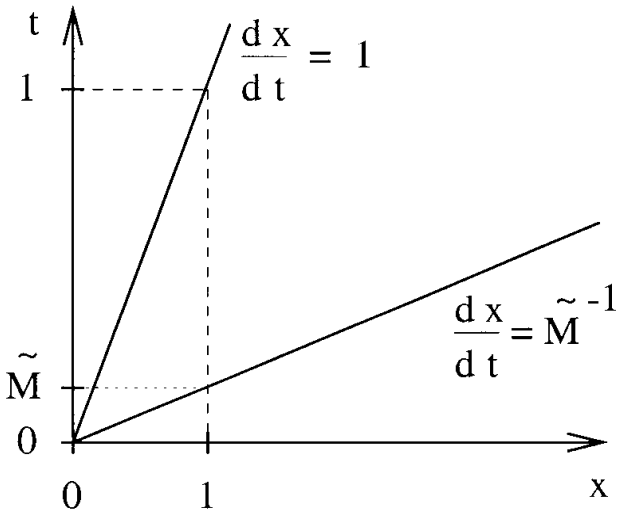

Figure 2: Characteristics in flow time.

analysis, each flow variable is expanded as e.g. the pressure

$$p(\mathbf{x},t,\tilde{M}) = p_0(\mathbf{x},t,\tau) + \tilde{M}p_1(\mathbf{x},t,\tau) + \tilde{M}^2p_2(\mathbf{x},t,\tau) + O(\tilde{M}^3) \tag{72}$$

with $\tau = \frac{t}{\tilde{M}}$ and $\tilde{M} = \frac{u^*_\infty}{\sqrt{p^*_\infty/\rho^*_\infty}}$.

The time derivative at constant $\mathbf{x}$ and $\tilde{M}$ involves the flow time derivative $\frac{\partial}{\partial t}$ and the acoustic time derivative $\frac{\partial}{\partial \tau}$:

$$\frac{\partial p}{\partial t}|_{\mathbf{x},\tilde{M}} = (\frac{\partial}{\partial t} + \frac{1}{\tilde{M}}\frac{\partial}{\partial \tau})[p_0 + \tilde{M}p_1 + \tilde{M}^2p_2 + O(\tilde{M}^3)] \tag{73}$$

The leading, first- and second-order continuity equations read

$$\frac{\partial \rho_0}{\partial \tau} = 0, \tag{74}$$

$$\frac{\partial \rho_1}{\partial \tau} + \frac{\partial \rho_0}{\partial t} + \boldsymbol{\nabla}\cdot(\rho\mathbf{u})_0 = 0, \tag{75}$$

$$\frac{\partial \rho_2}{\partial \tau} + \frac{\partial \rho_1}{\partial t} + \boldsymbol{\nabla}\cdot(\rho\mathbf{u})_1 = 0. \tag{76}$$

Equation (74) implies that ρ_0 does not depend on the acoustic time scale, i.e. $\rho_0 = \rho_0(\mathbf{x},t)$.

The leading, first- and second-order momentum equations are derived as

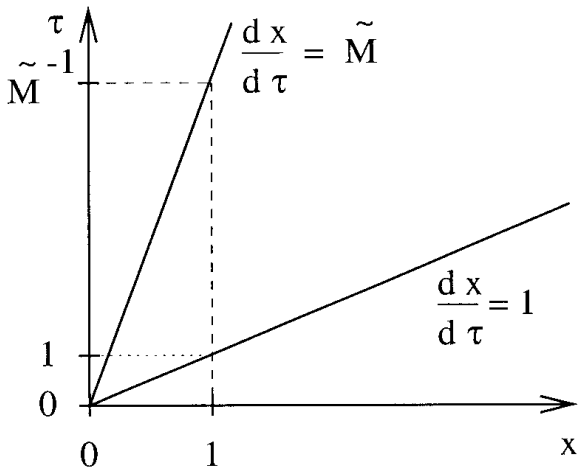

Figure 3: Characteristics in acoustic time.

$$\boldsymbol{\nabla} p_0 = 0, \tag{77}$$

$$\frac{\partial(\rho \mathbf{u})_0}{\partial \tau} + \boldsymbol{\nabla} p_1 = 0, \tag{78}$$

$$\frac{\partial(\rho \mathbf{u})_1}{\partial \tau} + \frac{\partial(\rho \mathbf{u})_0}{\partial t} + \boldsymbol{\nabla} \cdot (\rho \mathbf{u}\mathbf{u})_0 + \boldsymbol{\nabla} p_2 = \mathbf{G}_0 \tag{79}$$

with $\mathbf{G}_0 = \frac{1}{Re_\infty} \boldsymbol{\nabla} \cdot \boldsymbol{\tau}_0 + \frac{1}{Fr_\infty^2} \rho_0 (-\mathbf{e}_r)$
Because of equation (77), p_0 does not depend on $\mathbf{x}$, i.e. $p_0 = p_0(t, \tau)$.

The leading, first- and second-order energy equations yield

$$\frac{\partial(\rho E)_0}{\partial \tau} = 0, \tag{80}$$

$$\frac{\partial(\rho E)_1}{\partial \tau} + \frac{\partial(\rho E)_0}{\partial t} + \boldsymbol{\nabla} \cdot (\rho H \mathbf{u})_0 = Q_0, \tag{81}$$

$$\frac{\partial(\rho E)_2}{\partial \tau} + \frac{\partial(\rho E)_1}{\partial t} + \boldsymbol{\nabla} \cdot (\rho H \mathbf{u})_1 = Q_1 \tag{82}$$

with $\quad Q_0 = \frac{\gamma}{(\gamma-1) Re_\infty Pr_\infty} \boldsymbol{\nabla} \cdot (\kappa \boldsymbol{\nabla} T)_0 + (\rho q)_0$
and $\quad Q_1 = \frac{\gamma}{(\gamma-1) Re_\infty Pr_\infty} \boldsymbol{\nabla} \cdot (\kappa \boldsymbol{\nabla} T)_1 + (\rho q)_1$

Equation (80) implies that $(\rho E)_0 = (\rho E)_0(\mathbf{x}, t)$. Since the rate of work done by the viscous and buoyancy forces is of order $O(\tilde{M}^2)$, the zeroth- and first-order energy source

terms Q_0 and Q_1 are governed by heat conduction and heat release rate only, provided the Prandtl number Pr_∞ is of order $O(1)$ and the Froude number squared Fr_∞^2 is of order $O(Re_\infty Pr_\infty)$ assuming that the ratio $(\gamma-1)/\gamma$ is of order $O(1)$ in both cases. However, if the Reynolds number Re_∞ is of the order $O(\tilde{M}^2)$, i.e. the reference pressure p_∞^* is of the order of the viscous force per unit area $O(\mu_\infty^* u_\infty^*/L^*)$, or if the Froude number Fr_∞ is of the order $O(\tilde{M})$, i.e. the reference pressure p_∞^* is of the order of the hydrostatic pressure $O(\rho_\infty^* g^* L^*)$, then the rate of work done by the viscous or buoyancy forces, respectively, will also contribute to the zeroth-order energy source term Q_0.

For the algebraic equations, the asymptotic expansion yields the same relations as for the single scale asymptotic analysis (32) - 47).

Using the consequences of equations (77) and (80) in (38), we obtain for the zeroth-order pressure

$$p_0(t,\tau) = (\gamma-1)(\rho E)_0(\mathbf{x},t). \tag{83}$$

Consequently, the zeroth-order pressure p_0 and the zeroth-order total energy density $(\rho E)_0$ only depend on the flow time t, and we get

$$p_0(t) = (\gamma-1)(\rho E)_0(t). \tag{84}$$

Using the consequence of equation (74), the first-order momentum equation (78) can be simplified to

$$\frac{\partial \mathbf{u}_0}{\partial \tau} + \frac{1}{\rho_0}\boldsymbol{\nabla} p_1 = 0. \tag{85}$$

With $\rho_0 H_0 = (\rho E)_0 + p_0 = \frac{\gamma}{\gamma-1} p_0$, (38), and (39), the first-order energy equation (81) becomes

$$\frac{\partial p_1}{\partial \tau} + \gamma p_0 \boldsymbol{\nabla}\cdot\mathbf{u}_0 = (\gamma-1)Q_0 - \frac{dp_0}{dt}. \tag{86}$$

Subtracting the divergence of (85) multiplied by γp_0 from the acoustic time derivative of (86), i.e. $\frac{\partial}{\partial\tau}$ (86) $-\gamma p_0 \boldsymbol{\nabla}\cdot$ (85), yields (since $\frac{\partial}{\partial\tau}$ and $\boldsymbol{\nabla}\cdot$ commute)

$$\frac{\partial^2 p_1}{\partial \tau^2} - \boldsymbol{\nabla}\cdot(c_0^2 \boldsymbol{\nabla} p_1) = (\gamma-1)\frac{\partial(\rho q)_0}{\partial\tau}. \tag{87}$$

Note that $c_0^2 = \gamma\frac{p_0(t)}{\rho_0(\mathbf{x},t)}$ depends on $\mathbf{x}$ and t, but not on τ. Thus, (87) represents an inhomogeneous linear wave equation with nonconstant coefficient c_0^2. Its source is due to the acoustic time change of the zeroth-order heat release rate. The source of (87) is not affected by heat conduction, because the acoustic time derivative of the zeroth-order temperature $T_0 = p_0(t)/\rho_0(\mathbf{x},t)$ vanishes. The rate of work done by the viscous and buoyancy forces does not affect the first-order pressure p_1, unless the conditions $Re_\infty = O(\tilde{M}^2)$ or $Fr_\infty = O(\tilde{M})$, respectively, hold.

If the zeroth-order speed of sound c_0 is approximated by the ambient speed of sound c_∞ (with the ambient chosen as reference state), equation (87) constitutes the basic equation of thermoacoustics to describe acoustic effects in combustion [27], [28]. The acoustic time change of the heat release rate constitutes the dominant thermoacoustic source in combustion, as the right hand side of (87) is governed by the monopole source $(\gamma-1)\frac{\partial(\rho q)_0}{\partial\tau}$ [27], [28]. The governing equation of thermoacoustics, i.e. the simplification of (87) just

mentioned, can also be derived by simplifying Lighthill's acoustic analogy for combustion [27]. That equation can be solved analytically by means of Green's function [29].

The zeroth-order pressure p_0 can be determined by integrating equation (86) over the volume V of the computational domain as for the low Mach number equations [10]:

$$\frac{dp_0}{dt}\int_V dV + \gamma p_0 \int_{\partial V} \mathbf{u}_0 \cdot \mathbf{n} dA = (\gamma - 1)\int_V Q_0 dV - \int_V \frac{\partial p_1}{\partial \tau} dV. \tag{88}$$

Knowing $\mathbf{u}_0$ at the boundary of the computational domain or just the volume flow, knowing the heat conduction and heat release rate $\int_V Q_0 dV$ in the computational domain and assuming that the integrated effect of the acoustic time change of the first-order pressure is negligible, i.e. $\int_V \frac{\partial p_1}{\partial \tau} dV = 0$, the ODE (88) can be solved for $p_0(t)$ starting from an initial condition $p_0(0)$ as equation (68) for the low Mach number equations.

Equation (86), derived from the first-order energy equation, has an interesting consequence for the divergence of the zeroth-order velocity:

$$\boldsymbol{\nabla} \cdot \mathbf{u}_0 = \frac{\gamma - 1}{\gamma p_0} Q_0 - \frac{1}{\gamma p_0}[\frac{dp_0}{dt} + \frac{\partial p_1}{\partial \tau}]. \tag{89}$$

Thus, the divergence of $\mathbf{u}_0$ is affected by the heat conduction and heat release rate Q_0, the time change of the global pressure p_0 and the acoustic time change of the first-order pressure p_1.

Using the product rule in the first-order continuity equation (75) and inserting (89), the zeroth-order density change along the zeroth-order path line reads

$$\frac{\partial \rho_0}{\partial t} + \mathbf{u}_0 \cdot \boldsymbol{\nabla} \rho_0 = -\frac{\gamma - 1}{c_0^2} Q_0 + \frac{1}{c_0^2}\frac{dp_0}{dt} + \frac{\partial}{\partial \tau}(\frac{p_1}{c_0^2} - \rho_1). \tag{90}$$

Thus, the zeroth-order density of a fluid particle is changed by the heat conduction and heat release rate Q_0, the global pressure time change $\frac{dp_0}{dt}$ and by the acoustic time change of the first-order entropy, i.e. $\frac{\partial}{\partial \tau}(\frac{p_1}{c_0^2} - \rho_1)$.

1.6 Removal of Acoustics and Significance of Pressure

In this section, we discuss the removal of acoustics and the significance of the pressure in low Mach number flow. If the first-order continuity and energy equations and the second-order momentum equation of the previous multiple scales asymptotic analysis are averaged over an acoustic wave period, the averaged velocity tensor describes the net acoustic effect on the averaged flow field. Removing acoustics altogether leads to the low Mach number equations. The physical significance of the zeroth-, first- and second-order pressures is discussed.

We assume acoustic waves with period T_a such that $(\rho_1, (\rho \mathbf{u})_1, (\rho E)_1)^T(\mathbf{x}, t, \tau) = (\rho_1, (\rho \mathbf{u})_1, (\rho E)_1)^T(\mathbf{x}, t, \tau + T_a)$. Integrating equation (90) over a period T_a of the acoustic wave using $\int_0^{T_a} \frac{\partial}{\partial \tau}(\frac{p_1}{c_0^2} - \rho_1) d\tau = 0$, we obtain the simplification

$$\frac{\partial \rho_0}{\partial t} + \bar{\mathbf{u}}_0 \cdot \boldsymbol{\nabla} \rho_0 = -\frac{\gamma - 1}{c_0^2} \bar{Q}_0 + \frac{1}{c_0^2}\frac{dp_0}{dt}. \tag{91}$$

where the overbar denotes acoustic time averaging, i.e. $\bar{\mathbf{u}}_0(\mathbf{x}, t) = \frac{1}{T_a}\int_0^{T_a} \mathbf{u}_0(\mathbf{x}, t, \tau) d\tau$ for the averaged velocity.

Similarly, equation (89) can be simplified by integration:

$$\boldsymbol{\nabla} \cdot \bar{\mathbf{u}}_0 = \frac{\gamma - 1}{\gamma p_0} \bar{Q}_0 - \frac{1}{\gamma p_0} \frac{dp_0}{dt}. \tag{92}$$

Integrating the second-order momentum equation (79) over the acoustic wave period T_a, we get

$$\frac{\partial \rho_0 \bar{\mathbf{u}}_0}{\partial t} + \boldsymbol{\nabla} \cdot (\rho_0 \overline{\mathbf{u_0} \mathbf{u_0}}) + \boldsymbol{\nabla} \bar{p}_2 = \bar{\mathbf{G}}_0, \tag{93}$$

where the averaged velocity tensor $\overline{\mathbf{u_0} \mathbf{u_0}} = \frac{1}{T_a} \int_0^{T_a} \mathbf{u}_0(\mathbf{x}, t, \tau) \mathbf{u}_0(\mathbf{x}, t, \tau) d\tau$ describes the net acoustic effect on the averaged flow field. The solution of the averaged momentum equation (93) requires the knowlege of $\mathbf{u}_0(\mathbf{x}, t, \tau)$ over an acoustic wave period to determine $\overline{\mathbf{u_0} \mathbf{u_0}}$. In a numerical solution, we might be able to choose the numerical time step Δt equal to the acoustic wave period T_a and solve the inhomogeneous wave equation (87) by subdividing T_a into a number of acoustic time steps $\Delta\tau$ to obtain $p_1(\mathbf{x}, t, \tau + m\Delta\tau)$, $m = 1, ..., T_a/\Delta\tau$. Then, the numerical solution of (85) yields $\mathbf{u}_0(\mathbf{x}, t, \tau + m\Delta\tau)$, $m = 1, ..., T_a/\Delta\tau$. Finally, the averaged velocity tensor $\overline{\mathbf{u_0} \mathbf{u_0}}$ can be obtained by numerical integration.

If the averaged velocity tensor $\overline{\mathbf{u_0} \mathbf{u_0}}$ is approximated by the tensor $\bar{\mathbf{u}}_0 \bar{\mathbf{u}}_0$ of the averaged velocities, even the net acoustic effect is removed from (93) and we obtain the momentum equation in the zero Mach number limit:

$$\frac{\partial \rho_0 \bar{\mathbf{u}}_0}{\partial t} + \boldsymbol{\nabla} \cdot (\rho_0 \bar{\mathbf{u}}_0 \bar{\mathbf{u}}_0) + \boldsymbol{\nabla} \bar{p}_2 = \bar{\mathbf{G}}_0. \tag{94}$$

The averaged first-order continuity equation (75) yields

$$\frac{\partial \rho_0}{\partial t} + \boldsymbol{\nabla} \cdot (\rho_0 \bar{\mathbf{u}}_0) = 0. \tag{95}$$

Using (95) to express $\boldsymbol{\nabla} \cdot \bar{\mathbf{u}}_0$ and using the equation of state $p_0(t) = \rho_0(\mathbf{x}, t) T_0(\mathbf{x}, t)$, the energy equation (92) becomes

$$\frac{\gamma}{\gamma - 1} \rho_0 [\frac{\partial T_0}{\partial t} + \bar{\mathbf{u}}_0 \cdot \boldsymbol{\nabla} T_0] - \frac{dp_0}{dt} = \bar{Q}_0. \tag{96}$$

Equations (95), (94), (96) coincide with the low Mach number equations (64), (65), (66) derived by the single scale asymptotic analysis in section 1.4.

Contrary to the low Mach number equations, the intermediate equations (95), (93), (96) take the acoustic effect of the nonlinearity on the averaged flow in the momentum equation into account. It will be interesting to investigate the significance of (93) instead of (94), because like the low Mach number equations the intermediate equations (95), (93), (96) can be solved more easily than the compressible Navier-Stokes equations.

Since the zeroth-order pressure $p_0(t)$ serves as the mean pressure in the energy equation, it represents the global thermodynamic pressure part. As the second-order pressure $p_2(\mathbf{x}, t)$ is determined by the momentum equation as the pressure complying with the constraint (92) on the velocity divergence analogously to incompressible flow, $\tilde{M}^2 p_2(\mathbf{x}, t)$ may be called the 'incompressible' pressure part. The low Mach number momentum equation (94) is coupled to the low Mach number energy equation (96) via the density ρ_0, viscosity $\mu(T_0)$ and equation of state $p_0 = \rho_0 T_0$, whereas the first-order momentum and energy equations with acoustics included (85) and (86) are directly coupled by the

first-order pressure $p_1(\mathbf{x}, t, \tau)$. Since $p_1(\mathbf{x}, t, \tau)$ is governed by the inhomogeneous wave equation (87), $\tilde{M}p_1(\mathbf{x}, t, \tau)$ can be identified as the acoustic pressure part. These roles of the pressure are also identified by a single time scale, multiple space scale low Mach number asymptotics for the Euler equations [13]. In that analysis, long wave acoustics is described by a homogeneous wave equation for the first-order pressure after volume averaging the small flow scales.

Summarizing the multiple scales low Mach number asymptotic analysis, the pressure p can be split into the sum of

- $p_0(t)$, the large global thermodynamic pressure,
- $\tilde{M}p_1(\mathbf{x}, t, \tau)$, the small acoustic pressure,
- $\tilde{M}^2 p_2(\mathbf{x}, t, \tau)$, the very small 'incompressible' pressure,

and higher order terms of $O(\tilde{M}^3)$.

2 Numerical Implications

In section 2.1, the low Mach number asymptotics is used to recommend which equations to choose for modelling low Mach number flow. After discussing physical and numerical issues of computing low speed flow in section 2.2, numerical methods for low Mach number flow simulations are reviewed in section 2.3. In section 2.4, the perturbation form of the Navier-Stokes equations is introduced to avoid the cancellation problem in low Mach number flow computations. The characteristic based approximate Riemann solver explained in section 2.5 yields a simple flux evaluation and can be formulated without cancellation problems.

2.1 Choice of Equations

The low Mach number asymptotics of the Navier-Stokes equations gives a basic guidance which equations to choose for the numerical simulation of low Mach number flow. The asymptotic analysis shows that acoustic waves are inherent in the Navier-Stokes equations at low Mach numbers. Acoustics can be filtered out of the Navier-Stokes equations leading to the low Mach number equations. Alternatively, acoustics can be filtered out of the initial conditions such that the acoustic waves are not excited when solving the Navier-Stokes equations [30].

If we are interested in aeroacoustics, Lighthill's acoustic analogy gives insight into the sound generation by flow [29]. Lighthill's equation is the inhomogeneous wave equation for the acoustic density $\rho^{*\prime} = \rho^* - \rho_o^*$

$$\frac{\partial^2 \rho^{*\prime}}{\partial t^{*2}} - c_o^{*2} \Delta^* \rho^{*\prime} = \boldsymbol{\nabla}^* \cdot \boldsymbol{\nabla}^* \cdot \mathbf{T}^*, \tag{97}$$

which is derived without approximation from the continuity and momentum equations. The subscript o denotes the values in the undisturbed fluid. The source of (97) is a quadrupole, the strength of which is Lighthill's stress tensor $\mathbf{T}^*$ with the components

$$T_{ij}^* = \rho^* u_i^* u_j^* + (p^{*\prime} - c_o^{*2} \rho^{*\prime}) \delta_{ij} - \tau_{ij}^*, \tag{98}$$

where $p^{*\prime} = p^* - p_o^*$ is the acoustic pressure and τ_{ij}^* is the viscous stress. The Kronecker delta is defined by $\delta_{ij} = 1$, if $i = j$ and $\delta_{ij} = 0$, if $i \neq j$. $\mathbf{T}^*$ describes the sound generation due to flow nonlinearities. The sound propagation in the farfield is governed by the linear wave equation, because $T_{ij}^* = const$ there. Thus, Lighthill's equation (97) shows that the sound generation in flow is due to nonlinearities, whereas the sound propagation is in general linear. If we assume that the acoustic field does not affect the flow from which the sound originated, we can determine the source of sound and compute the acoustic density as if it were generated by that source in a fluid at rest. That approach is called the acoustic analogy [31], [32].

When the acoustic analogy is used, the incompressible Navier-Stokes equations are usually solved by a suitable CFD method in a small domain V, which contains the sources of sound. Having determined Lighthill's stress tensor (98), the analytical solution of Lighthill's equation (97)

$$\rho^{*\prime}(\mathbf{x}^*, t^*) \;=\; \frac{1}{4\pi(c_0^*)^2} \boldsymbol{\nabla}^* \cdot \boldsymbol{\nabla}^* \cdot \int_V \frac{\mathbf{T}^*(\mathbf{y}^*, t^* - |\mathbf{x}^* - \mathbf{y}^*|/c_0^*)}{|\mathbf{x}^* - \mathbf{y}^*|} dV(\mathbf{y}^*). \tag{99}$$

can be evaluated numerically.

Using Kirchhoff's theorem, the volume integral in (99) can be expressed as a surface integral. If the acoustic pressure and normal velocity is known on the boundary of V, that surface integral can be evaluated to determine the acoustic density in the farfield. The acoustic pressure follows from the isentropic relation $p^{*\prime} = (c_0^*)^2 \rho^{*\prime}$.

For aeroacoustic applications, the compressible Navier-Stokes and Euler equations, the linearized Euler equations and the wave equation require highly accurate numerical methods to compute the acoustic waves accurately and efficiently [33].

With the arguments on low Mach number asymptotics and on basic concepts of computational aeroacoustics [34], [35], [36], [33], we arrive at the following recommendations:

1. If you are *not interested in acoustic effects* in low Mach number flow, you may use the
   (a) low Mach number equations for combustion,
   (b) Boussinesq equations for free convection,
   (c) incompressible Navier-Stokes equations for constant density flows and the decoupled energy equation for forced convection.
2. If you are *not interested in viscous effects* in low Mach number flow, you may use the
   (a) Euler equations for nonlinear effects including inviscid sound generation and sound propagation,
   (b) potential equation for steady, irrotational and either isentropic or incompressible flow,
   (c) wave equation for linear acoustic effects in a fluid at rest.
3. If you are *only interested in acoustic effects* in low Mach number flow, you may use the
   (a) Navier-Stokes equations for nonlinear generation and propagation of sound as well as resonance,

(b) linearized Euler equations for linear propagation of sound; the Euler equations are linearized around a uniform mean flow or an unsteady incompressible Navier-Stokes solution,

(c) acoustic analogy or Kirchhoff's method for linear propagation of sound; the nonlinear sound generation is calculated from an incompressible or compressible Navier-Stokes solution,

(d) wave equation for linear propagation of sound in a fluid at rest; the sound generation is prescribed by initial and/or boundary conditions.

2.2 Physical Facts and Numerical Consequences

Physical and numerical issues of computing compressible low Mach number internal flow will be illustrated for slow flow through a symmetric Laval nozzle of length L and inlet (= outlet) diameter D (Fig. 4). Following Tam's review on CAA [35], special issues of external aeroacoustics will also be discussed.

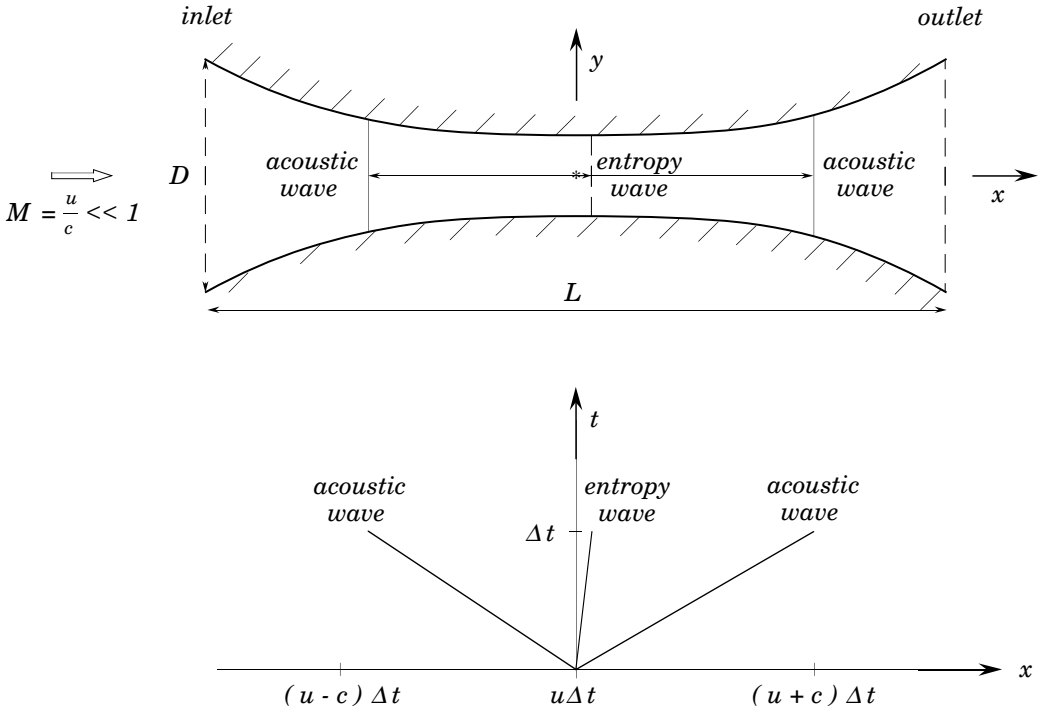

Figure 4: Acoustic and entropy waves generated by disturbance at $x = 0$ after time Δt for low Mach number M.

2.2.1 Large Disparity of Wave Speeds

We consider steady quasi-one-dimensional inviscid flow at a low Mach number

$$M = \frac{u^*}{c^*} \ll 1, \tag{100}$$

where u^* and c^* denote the dimensional x-velocity component and speed of sound, respectively. We assume flow from left to right, i.e. $u^* > 0$ and $M > 0$. The asterix indicating dimensional quantities is omitted in the figures.

If we disturb the flow at the throat $x^* = 0m$, we introduce an entropy wave travelling downstream with the flow velocity u^* and acoustic waves, one travelling downstream with the velocity $u^* + c^*$ and the other one travelling upstream with the velocity $u^* - c^*$. The ratio of the largest and smallest wave speeds is

$$\frac{u^* + c^*}{u^*} \;=\; 1 + \frac{1}{M} \quad \longrightarrow \infty \qquad for\ M \longrightarrow 0. \tag{101}$$

The large disparity of wave speeds corresponds to the large disparity of distances travelled by the acoustic and entropy waves during a time interval (Fig. 4).

If we use an explicit time stepping scheme to solve the quasi-1D Euler equations numerically, the time step Δt^* is limited by a stability condition of the form

$$\Delta t^*_{com} \;\leq\; \sigma \frac{\Delta x^*}{|u^*| + c^*}, \tag{102}$$

where Δx^* is the mesh spacing and $\sigma = O(1)$ the Courant number. For incompressible flow, acoustics is neglected, and the time step restriction is much less severe:

$$\Delta t^*_{inc} \;\leq\; \sigma \frac{\Delta x^*}{|u^*|}. \tag{103}$$

The reciprocal of the wave speed ratio (101) corresponds to the ratio of the allowable time steps for compressible and incompressible flow

$$\frac{\Delta t^*_{com}}{\Delta t^*_{inc}} = \frac{|u^*|}{|u^*| + c^*} = \frac{|M|}{1 + |M|} \quad \longrightarrow\ 0 \qquad for\ M \longrightarrow 0. \tag{104}$$

Thus for low Mach numbers, the acoustic waves require the time step of explicit schemes to be much smaller than for incompressible flow.

The wave speed ratio (101) corresponds to the ratio of the largest and smallest moduli of the eigenvalues of the flux Jacobian of the quasi-1D Euler equations. Thus, the Euler equations become ill-conditioned for $M \longrightarrow 0$. For multi-dimensional implicit factorization methods, the factorization error becomes very large for low Mach numbers, because its condition number, i.e. of the products of the flux Jacobians in the different coordinate directions, becomes excessive.

Many compressible flow solvers developed for transonic flow use a second-order central spatial discretization and add second- and fourth-order numerical damping scaled by the spectral radius of the flux Jacobian. The resulting artificial viscosity $(|u^*| + c^*)\Delta x^*$ for the quasi-1D Euler equations introduces much larger errors than the corresponding value $|u^*|\Delta x^*$ for incompressible flow. For matrix valued artificial viscosity and proper characteristic based upwind methods, similar conclusions hold.

2.2.2 Large Acoustic/Mean Flow Disparity

If we perturb the flow velocity u^* in the Laval nozzle (Fig. 4) by δu^*, we introduce upstream and downstream running acoustic waves, across which the transient pressure changes by

$$\frac{\delta p^*_{tra}}{p^*} = \mp \frac{\rho^* c^* \delta u^*}{p^*} = \mp \gamma M \frac{\delta u^*}{u^*} \quad \longrightarrow\ 0 \qquad for\ M \longrightarrow 0 \tag{105}$$

due to the characteristic relations, if the effects of the varying cross-section are neglected. For isentropic flow and constant cross-section, $c^* \pm \frac{\gamma - 1}{2} u^*$ are Riemann invariants on the

characteristics $\frac{dx^*}{dt^*} = u^* \pm c^*$. Thus, for entropy $s^* = const$, we obtain the transient temperature change in 1D flow of perfect gas

$$\frac{\delta T^*_{tra}}{T^*} = \frac{\delta c^{*2}}{c^{*2}} = \mp\frac{(\gamma-1)c^*\delta u^*}{c^{*2}} = \mp(\gamma-1)M\frac{\delta u^*}{u^*} \quad \longrightarrow\ 0 \qquad for\ M \longrightarrow 0. \tag{106}$$

Using the equation of state (10) for perfect gas, we obtain the transient density change

$$\frac{\delta \rho^*_{tra}}{\rho^*} = \mp M\frac{\delta u^*}{u^*} \quad \longrightarrow\ 0 \qquad for\ M \longrightarrow 0. \tag{107}$$

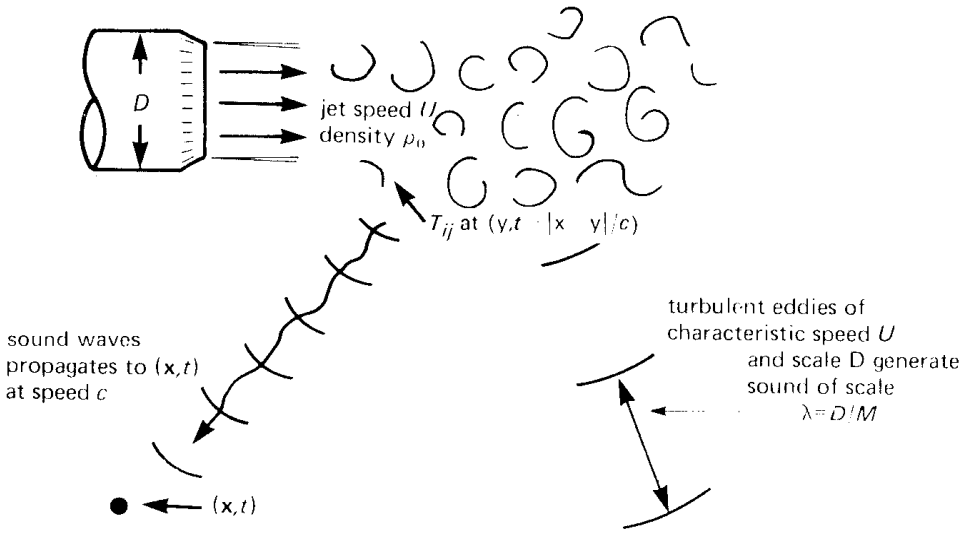

Figure 5: Sound generation by a low Mach number jet.

Let us consider the example of subsonic jet noise (Fig. 5 after [31]). Depending on the jet velocity, $120dB$ or even higher sound pressure levels can be measured in the farfield of the jet at about 50 jet diameters distance. That noise level corresponds to an acoustic pressure of $p^{*\prime} = 20Pa$. The ratio of acoustic to mean flow pressure $p^* \approx 10^5\, Pa$ is $O(10^{-4})$.

Assuming steady flow, the pressure, temperature and density changes induced by a velocity change δu^* are even smaller. Since the total enthalpy $H^* = \frac{c^{*2}}{\gamma-1} + \frac{1}{2}u^{*2}$ and entropy s^* are constant in steady quasi-1D inviscid flow without shocks, the Bernoulli equation yields the steady pressure change

$$\frac{\delta p^*_{ste}}{p^*} = -\frac{\rho^* u^* \delta u^*}{p^*} = -\gamma M^2\frac{\delta u^*}{u^*} \quad \longrightarrow\ 0 \qquad for\ M \longrightarrow 0. \tag{108}$$

The steady temperature change is derived from $H^* = const$

$$\frac{\delta T^*_{ste}}{T^*} = \frac{\delta c^{*2}}{c^{*2}} = -\frac{(\gamma-1)u^*\delta u^*}{c^{*2}} = -(\gamma-1)M^2\frac{\delta u^*}{u^*} \quad \longrightarrow\ 0 \qquad for\ M \longrightarrow 0. \tag{109}$$

With (10), the steady density change becomes

$$\frac{\delta\rho^*_{ste}}{\rho^*} = -M^2\frac{\delta u^*}{u^*} \quad \longrightarrow\ 0 \qquad for\ M \longrightarrow 0. \tag{110}$$

Computing small changes of large quantities leads to cancellation on the computer. From our previous analysis, the cancellation problem is more severe for simulations of steady flow than of transient flow. To avoid the accumulation of the cancellation errors, the perturbation form of the nonlinear equations is introduced in section 2.4 for compressible low Mach number computations.

The ratio of transient and steady-state pressure changes

$$\frac{\delta p^*_{tra}}{\delta p^*_{ste}} = \pm M^{-1} \quad \longrightarrow\ \infty \qquad for\ M \longrightarrow 0 \tag{111}$$

indicates that large transients arise in steady-state computations at low Mach numbers compared with the steady-state. The transients have to be damped and/or moved across the boundaries out of the domain of interest.

2.2.3 Large Length Scales Disparity

The large disparity of wave speeds in low Mach number flow can also be interpreted in terms of time or length scales (Fig. 4). If we consider viscous effects as well, another scale enters the problem. For high Reynolds numbers, the boundary layer thickness δ^* is much smaller than the diameter D^* of the nozzle. However, if we impose an acoustic field with angular frequency ω^*, another two length scales are introduced: the wave length $\lambda^* = \frac{2\pi c^*}{\omega^*}$ of the acoustic field and the acoustic boundary layer thickness $\delta^*_{ac} = \sqrt{\frac{2\mu^*}{\rho^*\omega^*}}$, across which the acoustic velocity $u^{*\prime} = u^* - u^*_\infty$ is reduced from $(1 - e^{-1})$ of its external value to zero at the wall. Fig. 6 after [37] shows $\delta_{ac} = \delta^*_{ac}/L^*$ for a flat plate boundary computation, where pressure waves were introduced at the outlet $x^*/L^* = 1$ ($M_\infty = 0.5$, $Re_\infty = \rho^*_\infty u^*_\infty L^*/\mu^*_\infty = 10000$, $\omega^* L^*/c^*_\infty = 20\pi/3$, $\Delta p^*/p^*_\infty = 0.0014$). Note that the nondimensional laminar boundary layer thickness $\delta = \delta^*/L^* = 5\sqrt{Re^{-1}_\infty} = 0.05$ at the outlet is far outside the plot.

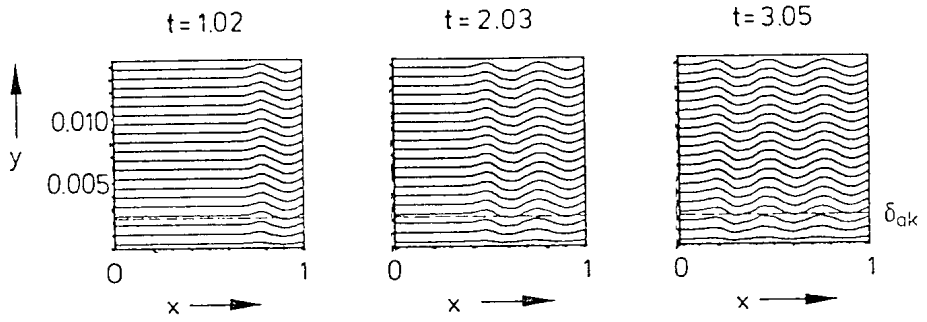

Figure 6: Acoustic velocity u' at different y locations in laminar flat plate boundary layer.

In general, we have the situation that the length scales are very disparate

$$\delta_{ac} \ll \delta \ll D \ll \lambda. \tag{112}$$

Thus close to the wall, the resolution must be even much finer than in the boundary layer, which already requires a finer grid than in the inviscid core region.

Broadband turbulent mixing noise is observed in the farfield of external flow. For example in the farfield of a subsonic turbulent jet, the frequency spans over two decades from $f^*_{min} \approx 300Hz$ to $f^*_{max} \approx 30000Hz$ [38]. Since the highest frequency f^*_{max} corresponds to the shortest wave length $\lambda^*_{min} = \frac{c^*_\infty}{f^*_{max}}$ of the sound waves,f^*_{max} determines the spatial resolution requirements. In the experiment of [38], $\lambda^*_{min} \approx 0.01m \approx \frac{1}{4}D^*$ where D^* is the nozzle exit diameter.

Suppose N_ϵ points suffice to resolve one wave length with an error of ϵ and we would use an isotropic grid point distribution in a $(100D)^3$ computational box, we would need $(100 \times 4 \times N_\epsilon)^3$ grid points to resolve the highest frequency of the sound waves in the farfield (not counting the additional points to properly resolve the nonlinear nearfield). As $N_{0.1} = 5$ for a sixth order central finite difference method [39], we would need 8 billion grid points. Even for Lele's spectral-like compact scheme with $N_{0.001} = 2.5$ [40], the number of grid points to resolve the farfield sound is excessive. However, since the farfield acoustic field is governed by the linear wave equation, more efficient methods are available to compute the farfield noise than direct numerical simulation.

As mentioned in section 2.1, Lighthill's acoustic analogy can be used to determine the farfield acoustic density by the exact solution (99) of the inhomogeneous wave equation (97). We have to calculate the volume integral of the quadrupole source of (97) evaluated at the retarded time when the sound was generated and divided by the distance between listener and source [29]. Approximations thereof for low Mach numbers, e.g. by Möhring [41], [42], are reviewed by Crighton [2]. The volume integral can be expressed as a surface integral using Kirchhoff's theorem [31]. Applications of the resulting Kirchhoff method in CAA are reviewed by Lyrintzis [34].

To predict the directivity and spectrum of the radiated sound in the farfield, the computed solution must be accurate throughout the entire computational domain. Thus, the accuracy requirements are much more severe then in conventional CFD, where usually only in the vicinity of the aerodynamic body accuracy is required. As the travelling distance from the sound source to the farfield is quite long (≈ 100 nozzle diameters for jet noise (Fig. 5) is realistic), the acoustic waves have to be accurately computed over a long propagation distance by direct numerical simulation. Thus, the numerical dispersion and dissipation errors have to be kept low from the nearfield to the farfield when using direct numerical simulation or up to a surface, beyond which the sound propagation is governed by the linear wave equation, when using Lighthill's acoustic analogy or Kirchhoff's method.

2.2.4 Boundary Conditions

At artificial boundaries, i.e. inflow, outflow and farfield, the boundary conditions should allow the acoustic waves travelling at the velocity $\mathbf{u}^* + c^*\mathbf{n}$ in any direction $\mathbf{n}$ and the entropy and vorticity waves travelling at the flow velocity $\mathbf{u}^*$ to leave the computational domain with minimal reflection in order to mimic an infinite domain. Otherwise the reflections will corrupt the results. In the inviscid flow regions, the non-reflecting boundary conditions developed for the Euler equations can be used [43], [44], [45], [46], [47], [48], [49],[50], pp. 387-395, [51],[52], [53], [54], [55], [14]. For the Navier-Stokes equations more information is required at the artificial boundaries than for the Euler equations [56], [57], [58], [59], [60], [61], [62].

For low Mach number flow, the acoustic waves travel about M^{-1} times faster than the entropy and vorticity waves. Therefore, any reflected wave will very quickly corrupt the

entire flow field. Thus, the proper boundary treatment of the acoustic waves is particularly important for low Mach number flow.

The significance of non-reflecting boundary conditions for the accuracy of unsteady flow and the convergence of steady flow was demonstrated by Müller [55], [14] for internal flow. Prescribing the pressure $p = p_{ambient}$ at the outlet leads to complete reflection of an acoustic wave, i.e. a right going acoustic wave is reflected at the outlet boundary as a left going acoustic wave with the same amplitude. Prescribing the entropy $s = s_0$ at the inlet corresponds to a non-reflecting boundary condition for the entropy wave, i.e. $\frac{\partial p}{\partial t} - c^2 \frac{\partial \rho}{\partial t} = 0$ at the inlet, cf. (139). However, prescribing the total enthalpy $H = H_0$ leads to almost complete reflection of an acoustic wave, i.e. a left going acoustic wave is reflected at the inlet boundary as a right going acoustic wave with the amplitude reduced by the factor $\frac{1-M}{1+M}$ [55], [14]. For low Mach numbers M, that factor is close to 1, i.e. close to complete reflection. The reflection of the acoustic waves at outlet and inlet in low Mach number flow is sketched in the x-t-diagram in Fig. 7. Even after the entropy wave has left the outlet without reflection, the acoustic waves continue to bounce back and forth. Their amplitude is only slightly reduced at the inlet.

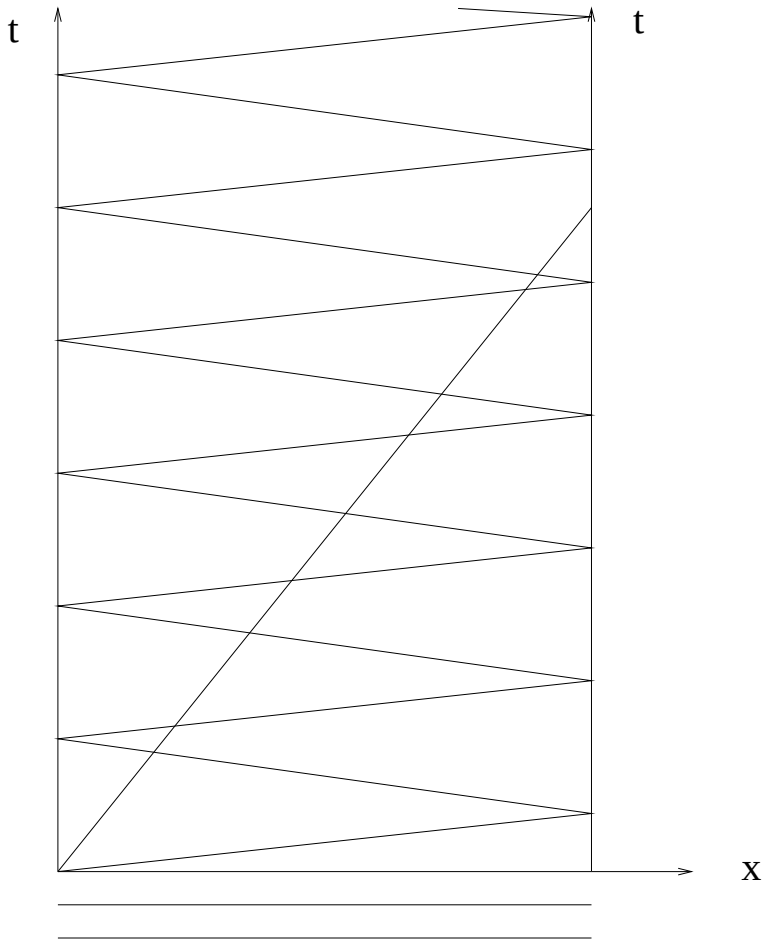

Figure 7: Reflection of acoustic waves at outlet and inlet in low Mach number flow.

These findings are confirmed by the computation of an acoustic pulse in a 1D tube using the Euler equations. The Mach number of the initially uniform flow is $M_0 = 10^{-2}$.

A pressure pulse is imposed at the outlet $x^* = L^*$ during $0 \leq t^* \leq t_p^*$ as in [63]:

$$p^*(L^*, t^*) = p_0^*(1 + \epsilon \, sin^4(\pi t^*/t_p^*)) \tag{113}$$

with $t_p^* = \frac{1}{3}\frac{L^*}{c_0^* - u_0^*}$ and $\epsilon = 10^{-2}$. 241 equidistant grid points are used. The time step of $\frac{\Delta t^*}{L^*/c_0^*} = 1.25 \times 10^{-3}$ corresponds to a maximum Courant number of 0.303. Fig. 8 shows the acoustic pressure at six time instants when using the reflecting inlet boundary conditions mentioned above. At $\tau = \frac{t^*}{L^*/c_0^*} = 1$, the acoustic pulse (cf. solid line in plot) has travelled from the outlet close to the inlet. At $\tau = 1.1$, the shape of the acoustic wave is altered by the reflecting boundary conditions. At $\tau = 1.2$, the acoustic pressure has changed sign. For $\tau = 1.3, 1.4$ and 1.5, we observe the reflected acoustic wave travelling towards the outlet.

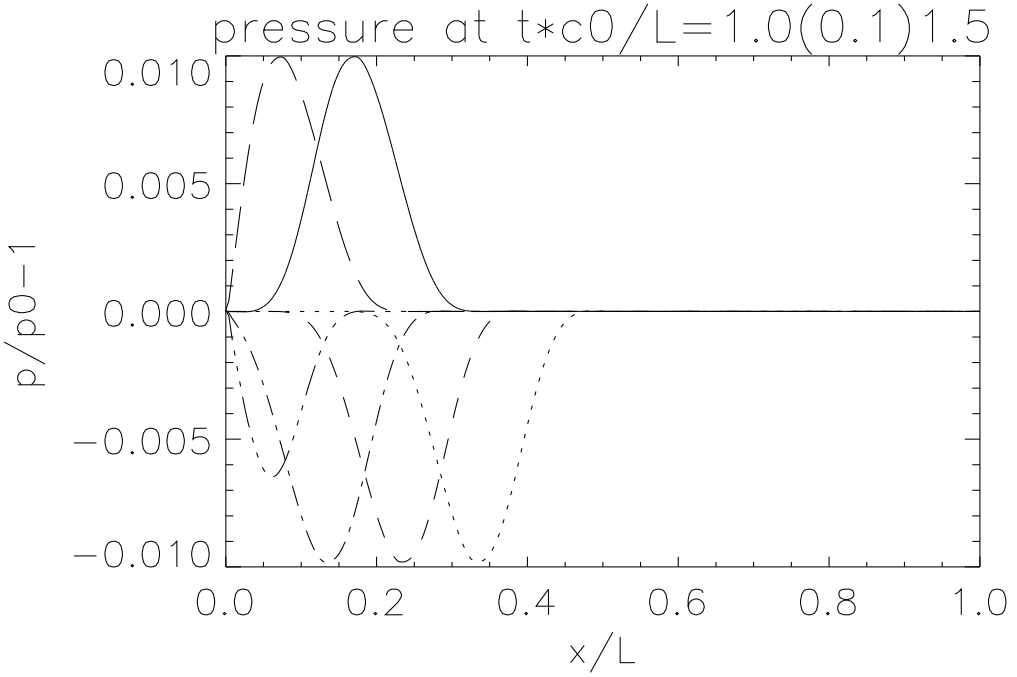

Figure 8: Acoustic pressure for acoustic pulse reflected at the inlet computed with reflecting boundary conditions.

The non-reflecting boundary conditions require the incoming characteristic variables not to change and the outgoing ones to be determined from the interior [43]. With non-reflecting boundary conditions, the inlet becomes permeable for the acoustic wave. It traverses the inlet with almost no reflection, as Fig. 9 illustrates. The acoustic pressure after $\tau = 1.4$ is almost zero. Actually, it is about 5 orders of magnitude lower than with reflecing boundary conditions.

For steady low Mach number flow, non-reflecting boundary conditions are decisive for the convergence, because with reflecting boundary conditions the acoustic waves are reflected at inlet and outlet and only reduced due to viscosity and a small reduction when interacting with the inlet for $H = H_0$. We consider the quasi-1D inviscid flow in a Laval nozzle with the cross-sectional area

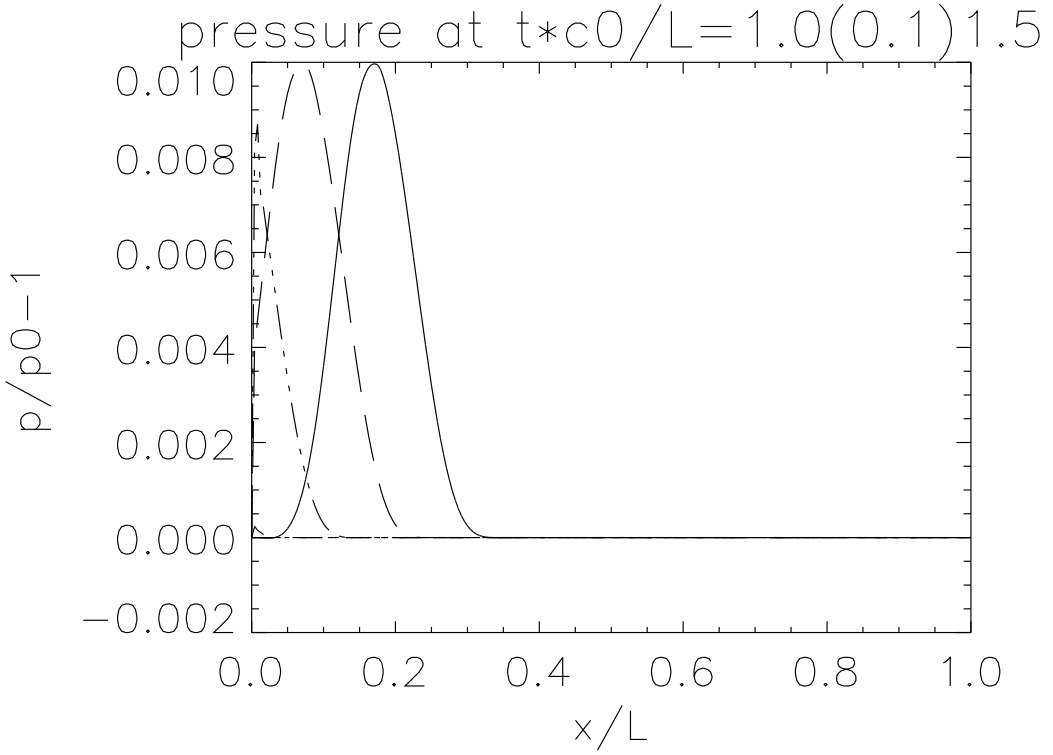

Figure 9: Acoustic pressure for acoustic pulse leaving the inlet computed with non-reflecting boundary conditions.

$$A(x) = \begin{cases} 1.75 - 0.75cos(2\pi(x-0.5)) & for \quad 0 \le x \le 0.5 \\ 1.25 - 0.25cos(2\pi(x-0.5)) & for \quad 0.5 \le x \le 1 \end{cases} \tag{114}$$

For $\frac{p^*_{outlet}}{p^*_0} = 0.999$, the Mach number is between 0.02 and 0.06. The quasi-1D Euler equations are solved using 101 equidistant grid points and a Courant number of 0.9. A linear distribution of ρ^*, u^* and p^* between the exact inlet and outlet values is chosen as initial condition. The convergence history $||\Delta(\rho^* E^*)^{n-1}/p^*_0||_2$ (Fig. 10) shows the poor convergence with the reflecting boundary conditions and the good convergence with non-reflecting boundary conditions, when using the first-order explicit Roe scheme. The residual of 10^{-7} corresponds to machine accuracy of 32 bit arithmetic employed in this test case.

At any boundary, the boundary conditions should be discretized in such a way that the overall accuracy of the numerical method is maintained. For higher order accurate methods this requirement needs special care. For higher order finite difference methods, higher order accurate non-central difference formulae are derived by Taylor expansions [40] or by satisfying the summation by parts rule, which guarantees stability by means of the energy method [39].

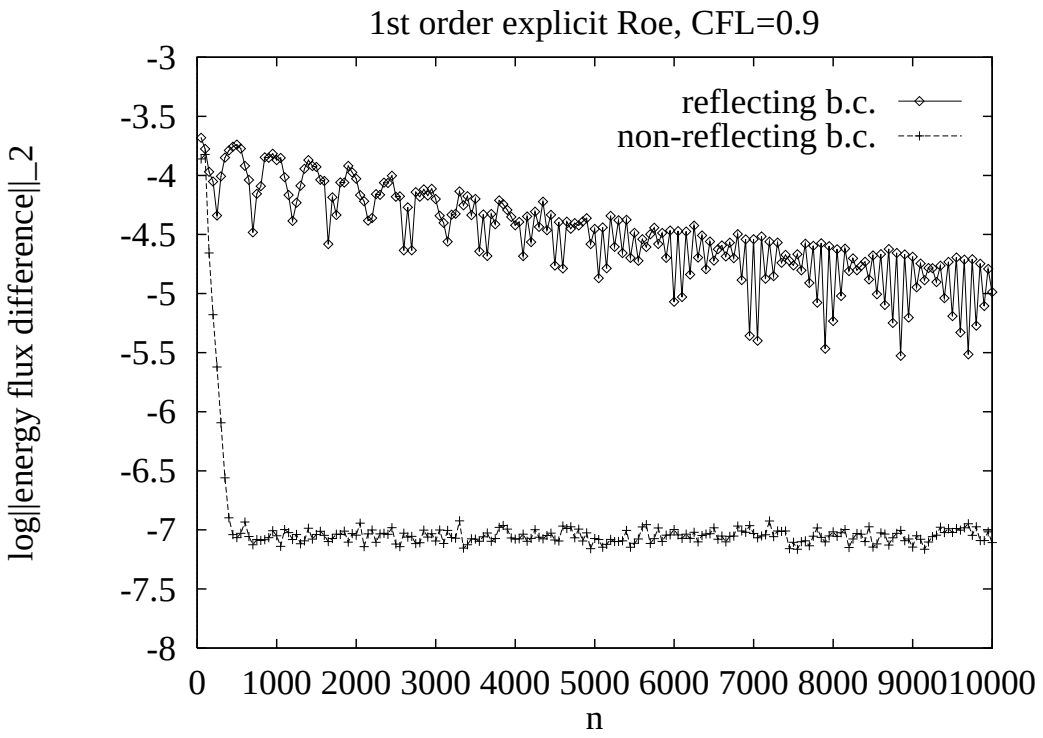

Figure 10: Convergence history for Laval nozzle ($0.02 < M < 0.06$).

2.3 Literature Review

Excellent introductions to aeroacoustics are provided by Lighthill [64], Dowling and Ffowcs Williams [31], Landau and Lifshitz [65], chapter 8, and others. Acoustics in a broader sense is treated e.g. by Pierce [66]. Brief reviews on the emerging field of computational aeroacoustics are given by [35] and [67], chapter 9. The proceedings of a recent workshop on CAA [68] may serve as an introduction.

In the direct numerical simulation of aerodynamic noise, central finite difference discretizations are preferred, because they avoid dissipation errors [69]. Since higher order difference approximations are more efficient than the conventional second-order central scheme to compute wave propagation (cf. e.g. [39], chapter 3), the former are favoured in CAA [35]. As mentioned in section 2.2.3, even more accurate compact finite-difference methods with fourth-order formal accuracy but spectral-like resolution were devised [40]. The dispersion error can be further minimized for long time integration by taking the initial values into account [70]. Explicit Runge-Kutta and Adams-Bashforth methods are optimized to keep the dissipation and dispersion errors due to time integration low [71], [54]. Thomas and Roe [72] devised an upwind variant of the leapfrog scheme, which is non-dissipative and has low dispersion error. In multi dimensions, finite difference methods introduce anisotropy errors, because for example in 2D the numerical phase velocity in the directions $m\pi/4$, m odd, is larger and more accurate than in the directions $m\pi/4$, m even [73], chapter 10. Averaging the difference operators in the transverse directions helps to reduce the anisotropy error at the expense of a wider stencil [73]. Streng, Kuerten, Broeze, and Geurts [74] developed a fourth-order accurate difference method of that kind for the direct numerical simulation of compressible flow. In order to avoid numerical contamination by the unresolved waves with very short wave lengths, these waves and only these

should be damped by added higher order numerical damping for central discretizations [39], [35] or by using higher order upwind discretizations.

Besides the explicit higher order difference methods developed for the direct numerical simulation of aeroacoustics, there are also other techniques usually developed for efficient second-order accurate computations of steady and/or unsteady low Mach number computations. Often, the density-based 'compressible' methods have originally been developed for transonic flow simulations and lately been applied to low Mach number flow [3]. The pressure-based 'incompressible' techniques have recently been extended from incompressible to compressible flow [75], [76], [77], [78], [79], [80], [81], [82]. According to [83], the simultaneous solution of the conservation laws in 'compressible' methods enhances stability compared with the sequential solution approach of 'incompressible' techniques, which employ a Poisson equation for the pressure instead of the continuity equation. Here, we shall focus on 'compressible' methods.

Time derivative preconditioning can be used to accelerate the convergence to steady-state for low Mach numbers , because the condition number of the modified inviscid system is brought close to 1 instead of M^{-1} for the Euler equations, e.g. [84]. Since the numerical damping added to central discretizations and inherent in upwind schemes scales with the condition number, the associated numerical damping error is much lower with the preconditioned system than with the original one for small M. The improved condition number allows more efficient applications of implicit methods, e.g. [85], [86], [87]. As the eigenvalues of the modified system are brought close to each other compared with the original disparity, smoothing of all waves and not just the fastest ones renders multigrid methods more efficient for the preconditioned system than for the original one, e.g. [88], [89], [90]. Using dual time stepping for unsteady flow simulation, the preconditioned system is iterated to steady-state in pseudo-time for each physical time step using a strongly implicit technique by [91]. Eriksson devised a preconditioning for low speed combustion [92]. For viscous flow, Choi and Merkle also take the cell Reynolds number $\frac{\rho u \triangle x}{\mu}$ into account [93], [94]. An excellent review on matrix and differential preconditioning is given by Turkel [95]. The recent developments are addressed by other lecturers at this "30th Computational Fluid Dynamics" VKI Lecture Series.

Implicit methods and *multigrid methods* yield convergence acceleration even without preconditioning. Using Jameson's multigrid finite volume method with residual smoothing and Pulliam and Steger's implicit finite difference method based on approximate factorization, Volpe was able to compute steady flow over a circular cylinder at $M_\infty = 0.1, 0.01$, and 0.001 [3]. However, accuracy and convergence problems were encountered for $M_\infty \longrightarrow 0$. Similar conclusions were drawn from quasi-1D inviscid Laval nozzle computations at low Mach numbers, when using an implicit upwind scheme [96], [97] and a multigrid acceleration of an explicit upwind scheme [98]. Implicit methods can also be used for unsteady flow computations at low Mach numbers. For example, Chen and Pletcher [99] compute unsteady flow over a circular cylinder with a strongly implicit procedure formulated for $p, \mathbf{u}$, and T.

Semi-implicit methods have mainly been devised for unsteady flow simulations. Gustafsson and co-workers use the new variable $\Phi = \frac{2}{\gamma-1}\frac{c^*-c^*_\infty}{u^*_\infty}$ to symmetrize the isentropic Euler and Navier-Stokes equations, which reduce to the incompressible flow equations for $M_\infty \to 0$ [100], [101], [102]. The resulting symmetric system is solved by a semi-implicit central difference scheme: the terms of $O(M_\infty^{-1})$ are discretized in time by the implicit Euler method, while the leapfrog scheme or an explicit one-step method is used for the

other terms of $O(1)$. Casulli and Greenspan [103] and Patnaik et al. [104] have shown that only the pressure and velocity terms in the momentum and energy equations, respectively, have to be treated implicitly to remove the sound speed restriction on the time step (102). Thus, the implicit part of these semi-implicit algorithms consists of an elliptic equation for the pressure correction. The 'incompressible' pressure is determined in a similar way by Klein, Munz, and co-workers [13], [105]. In their multiple pressure variable approach, not only advection of mass and momentum but also long wave acoustics are discretized by explicit upwind schemes. These methods can be viewed as extensions of the projection method from incompressible to compressible flow [105]. Most of the compressible flow extensions of the 'incompressible' methods mentioned above are based on the SIMPLE (i.e. semi-implicit method for pressure linked equations) approach using a pressure correction equation and solving the momentum and energy equations implicitly one after the other. To overcome the stability restriction (102), Zienkiewicz and co-workers treat the velocity and pressure derivatives implicitly in their non-conservative semi-implicit finite element method [106], [107]. In the implicit-explicit Godunov method of Collins et al., the intermediate states at the cell boundaries are advanced implicitly, if the local Courant number exceeds 1, and explicitly otherwise [108].

Flux-vector splittings treat the stiff terms not only differently in time but also in space. Erlebacher et al. split the linear acoustic equations from the Navier-Stokes equations and solve them analytically in Fourier space [109]. Abarbanel et al. split the speed of sound squared in $p = c^2\rho/\gamma$ as $c^2 = (c^2 - c_\infty^2) + c_\infty^2$ [110]. Sesterhenn et al. treat the resulting non-stiff part explicitly by an upwind method and the stiff part implicitly by a central discretization [97]. In the convection-pressure splitting by Rubin and Khosla and by Sesterhenn et al., the convection of mass, momentum and total enthalpy is discretized by an upwind method, whereas the pressure gradient in the momentum equation is approximated by a downwind method [111], [97]. Using an explicit time splitting implementation, that method and the semi-implicit speed of sound splitting proved to be more accurate than the Roe upwind scheme for steady quasi-1D inviscid Laval nozzle flow at low Mach numbers [97]. Since the explicit convection-pressure splitting led to stability problems when applied in the transverse direction of a 2D nozzle, the modifications introduced with similar but more general flux-vector splittings by Liou and Steffen [112] and by Jameson [113] seem to be essential.

Perturbation techniques have been employed for steady and unsteady flow calculations. For very low Mach numbers of $O(10^{-2})$ to $O(10^{-5})$, Merkle and Choi use asymptotic expansions of the Euler equations in terms of γM_∞^2 and solve the zeroth-order equations by an implicit method [114]. Dadone and Napolitano report a considerable improvement in accuracy, especially in stagnation point regions, by a perturbative formulation of Moretti's λ-scheme using an incompressible potential flow solution [115]. Solving for the conservative perturbation variables and avoiding cancellation due to the flux evaluation, Sesterhenn was able to compute an expansion wave in a long thin tube accurately at $M_\infty = 10^{-11}$ [98], [116], cf. section (2.5).

2.4 Perturbation Form

Whereas the linearized Euler equations are solved for ρ', $\mathbf{u}'$ and p', i.e. the deviations of the primitive variables from a mean flow, by [54], [35], [71], [72], the conservative variables ρ, $\rho\mathbf{u}$ and ρE are the common choice of unknowns in compressible flow simulations, e.g. [69], [74]. Contrary to the density-based 'compressible' methods, the pressure-based

'incompressible' methods use the primitive variables p, $\mathbf{u}$ and T. Briley, McDonald and Shamroth [117] use $\tilde{p} = \frac{p^* - p^*_\infty}{\rho^*_\infty u^{*2}_\infty}$ for the isenthalpic Euler equations instead of $p = \frac{p^*}{\rho^*_\infty u^{*2}_\infty}$ or $p = \frac{p^*}{p^*_\infty}$ to avoid the singularity

$$\frac{p^*_\infty}{\rho^*_\infty u^{*2}_\infty} = \frac{1}{\gamma M^2_\infty} \longrightarrow \infty \quad for\ M_\infty \longrightarrow 0 \tag{115}$$

or vanishing velocity

$$\frac{u^*_\infty}{c^*_\infty} = M_\infty \longrightarrow 0 \quad for\ M_\infty \longrightarrow 0. \tag{116}$$

Hafez, Soliman and White [118] employ the nondimensional variables $\tilde{p}$, $\frac{\mathbf{u}^*}{u^*_\infty}$, and the reciprocal of the Eckert number $\frac{1}{Ec} = \frac{c^*_p(T^* - T^*_\infty)}{u^{*2}_\infty}$ to recover the incompressible equations from the compressible ones for $M_\infty \to 0$ and isothermal flow. For variable density, Hafez, Soliman and White [118] use the nondimensional temperature $\frac{T^*}{T^*_\infty}$ instead of the reciprocal of the Eckert number. Bijl and Wesseling [82] employ $\tilde{p}$, $\frac{\mathbf{u}^*}{u^*_\infty}$ and the nondimensional enthalpy $h = \frac{c^*_p T^*}{c^*_{p\infty} T^*_\infty}$. For constant c^*_p, the latter formulation by Hafez, Soliman and White [118] and the formulation by Bijl and Wesseling [82] coincide. With either formulation for variable density flow, the singularity of the conventional formulations of the compressible flow equations is avoided and the low Mach number equations with constant zeroth-order pressure $p^*_0 = p^*_\infty$ are recovered for $\tilde{M} = 0$. If we neglect the $O(\tilde{M}^3)$ term in the ansatz (63) and regard (63) as the definition of p_2, we get the relation $\frac{p^*_2}{p^*_\infty} = \tilde{p}$.

Sesterhenn et al. [98], [116] retain conservativity by solving for ρ', $(\rho\mathbf{u})'$ and $(\rho E)'$, i.e. the changes of the conservative variables with respect to their stagnation values. With these variables, the cancellation problem of the conventional conservative formulation is avoided in an application to nonlinear acoustics [98], [116], as we shall see now.

Since the changes of the thermodynamic variables in low Mach number flow (only pressure in low speed combustion) are much smaller than the thermodynamic variables themselves, the discretization of $\frac{\partial \rho}{\partial t}$, $\boldsymbol{\nabla} p$ and $\frac{\partial(\rho E)}{\partial t}$ will lead to cancellation. Let us illustrate the problem for the discretization of $\frac{\partial p}{\partial x}$ in 1D. No matter whether we use finite differences, volumes or elements, we have to compute pressure differences of the form

$$\Delta p \ = \ p_R - p_L. \tag{117}$$

For a cell-centered finite volume method, p_R and p_L may be the pressures at the right and left interfaces of a cell. From our nondimensionalization (13), the asymptotic expansions (63) and (72) and the estimates (105) and (108), we know that p_R and p_L are of order $O(1)$, while Δp is of the order $O(M)$ and $O(M^2)$ for unsteady and steady flows, respectively. We denote the relative errors of p_R and p_L by ϵ_R and ϵ_L, respectively, i.e. the numerical approximations $\widetilde{p_L}$ of p_L and $\widetilde{p_R}$ of p_R are

$$\widetilde{p_L} \ = \ p_L(1 + \epsilon_L), \qquad \widetilde{p_R} \ = \ p_R(1 + \epsilon_R). \tag{118}$$

Thus, we obtain for the numerical approximation $\widetilde{\Delta p}$ of Δp

$$\widetilde{\Delta p} \ = \ \widetilde{p_R} - \widetilde{p_L} \ = \ \Delta p(1 + \frac{p_R}{\Delta p}\epsilon_R - \frac{p_L}{\Delta p}\epsilon_L). \tag{119}$$

The condition numbers $\frac{p_R}{\Delta p}$ and $\frac{p_L}{\Delta p}$ are large for low Mach number flow. More precisely, they are of order $O(M^{-1})$ and $O(M^{-2})$ for unsteady and steady flow, respectively. Since

the relative errors ϵ_L and ϵ_R are in general neither nearly equal nor zero, the relative error of $\widetilde{\Delta p}$ is of the order $O(M^{-1})$ and $O(M^{-2})$ for unsteady and steady flow, respectively, because of (119). The accumulation of these errors can render low Mach number computations completely incorrect.

If we only consider the error due to the floating point representation of p_L and p_R, the relative errors are bounded by the machine accuracy ϵ_m of the computer used for the computation, i.e. $|\epsilon_L| \leq \epsilon_m$ and $|\epsilon_R| \leq \epsilon_m$. For IEEE (= Institute of Electronic and Electric Engineers) binary floating point systems, $\epsilon_m = 2^{-24} \approx 10^{-7}$ for single precision and $\epsilon_m = 2^{-53} \approx 10^{-16}$ for double precision [119]. Assuming that the floating point subtraction $\widetilde{p_R} - \widetilde{p_L}$ does not introduce an error (that relative floating point error is bounded by ϵ_m anyway), equation (119) describes the floating point error of $\widetilde{\Delta p}$ due to the floating point errors of $\widetilde{p_R}$ and $\widetilde{p_L}$. Using the bound ϵ_m of ϵ_L and ϵ_R in (119), we can then estimate the relative floating point error of $\widetilde{\Delta p}$ by

$$\left| \frac{\widetilde{\Delta p} - \Delta p}{\Delta p} \right| \leq \frac{p_R + p_L}{\Delta p} \epsilon_m. \tag{120}$$

Thus, for unsteady and steady low Mach number flow the relative error of $\widetilde{\Delta p}$ is of the order $O(M^{-1}\epsilon_m)$ and $O(M^{-2}\epsilon_m)$, respectively.

For example, a pressure difference evaluation at $M = 10^{-6}$ in IEEE single precision has a relative error of the order $O(10^{-1})$ for unsteady flow and even $O(10^5)$ for steady flow.

The large relative error in (120) is due to cancellation: subtracting two almost equal numbers leads to cancellation of the leading equal digits and leaves the difference of the remaining digits. However, if these remaining digits lie in the round-off error ranges of the two numbers, their difference only contains round-off errors. That is certainly true for steady flow in our previous example with $M = 10^{-6}$, where the steady pressure difference with single precision is completely incorrect. For unsteady flow, we are left with one correct significant digit only.

Let us investigate the effect of the cancellation error for the calculation of an expansion wave in a long thin tube, cf. Fig. 11. Aebli and Thomann provide experimental and analytical results [120]. Initially, the flow in the tube is at rest and under a little higher pressure $p_0^* + \Delta p_0^*$ than the ambient pressure p_0^*. The tube of $6mm$ diameter and about $100m$ length is closed at the right end. When the diaphragm at the left end is removed, an expansion wave runs into the tube expelling gas from the tube. For low Mach number flow, the thickness Δx of the inviscid expansion wave is very small and considerably exaggerated in Fig. 11. However, due to viscous effects in the thin tube, the pressure drops smoothly from $p_0^* + \Delta p_0^*$ to p_0^* at the outlet.

Sesterhenn used an explicit second-order cell-centered finite volume method for the discretization of the axisymmetric Navier-Stokes equations. For an outflow Mach number $M = 10^{-6}$, the numerical simulation led to an absolute error of the order $O(1)$, i.e. 100%, for the time dependent pressure $\hat{p} = (p^* - p_0^*)/\Delta p_0^*$ at a certain x^* location, as we can see in Fig. 12 [98]. We refer to the finite volume solution as conservative formulation. The nondimensional time and length scale variables are defined by [120], [98] as $\hat{t} = t^* \nu_0^* / R^{*^2}$ and $\hat{x} = x^* \nu_0^* / (c_0^* R^{*^2})$ with $R^* = 0.003m, p_0^* = 96170Pa, \rho_0^* = 1.13kg/m^3, \nu_0^* = 1.6 \times 10^{-5} m^2/s$.

The pressure computed with single precision using the conservative form is plotted in Fig. 13 [98] and compared with the approximate analytical solution by Aebli and

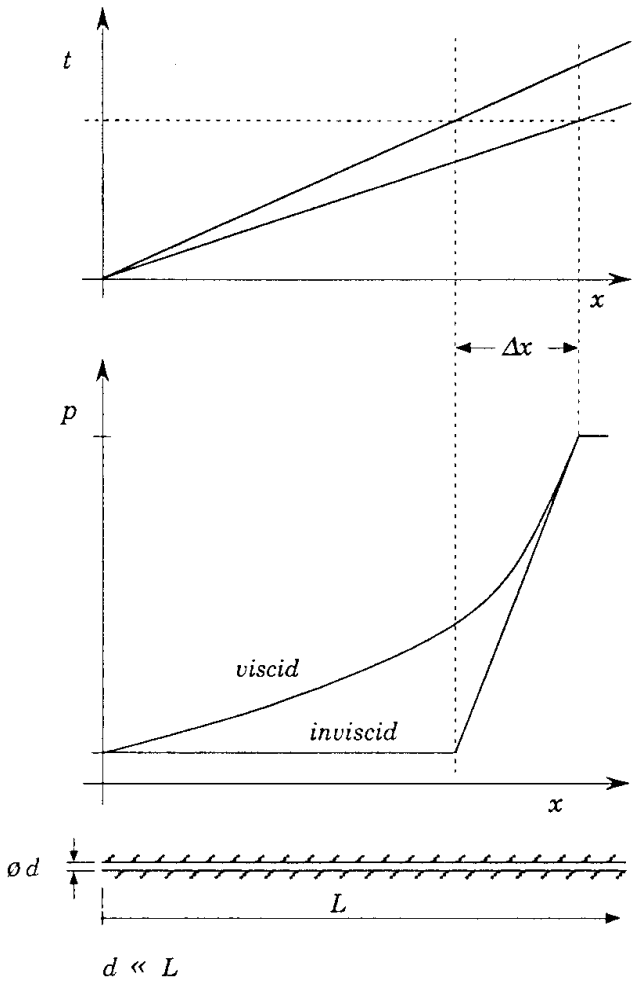

Figure 11: Sketch of an expansion wave in a long thin tube.

Thomann[120] at the same x^* location as in Fig. 12. In Fig. 14 [98], the computed and the analytical nondimensional pressures $\hat{p}$ are compared at a certain time instant. The computed results are completely incorrect, almost random.

Even at an outflow Mach number of $M = 0.01$, we observe clear errors in the pressure (Fig. 15) and the entropy along the axis of the tube (Fig. 16) with the conservative formulation [98], [116]. The results were obtained with 400×8 cells and using single precision. Here, we obtain the correct results with double precision for the entropy (Fig. 16) and pressure (not shown). Thus, the results with single precision reflect the round-off errors due to cancellation when using the conventional conservative formulation. Of course, we can use double precision to alleviate the cancellation problem. But the accuracy is reduced. The cancellation errors can accumulate and will show up for lower Mach numbers anyway.

How can we avoid cancellation? We have to reduce the condition numbers $\frac{p_L}{\Delta p}$ and $\frac{p_R}{\Delta p}$ in (119) from $O(M^{-1})$ or $O(M^{-2})$ to $O(1)$! How can we achieve that? By working with the pressure perturbation

$$p'(\mathbf{x}, t) \;=\; p(\mathbf{x}, t) - p_0 \tag{121}$$

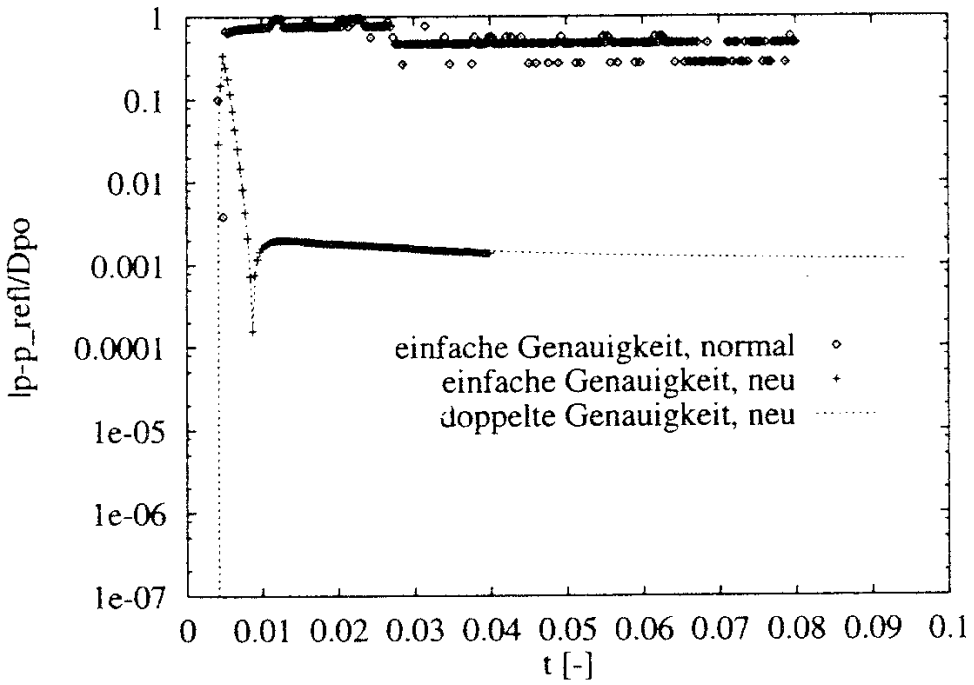

Figure 12: Error of computed pressure at an x location for $M = 10^{-6}$, $\diamond$: conservative formulation and single precision, $+$: perturbation formulation and single precision, $\cdots$: perturbation formulation and double precision.

with respect to the stagnation pressure p_0 instead of working with the pressure p itself. Since we assume constant stagnation conditions, we have $\frac{\partial p}{\partial x} = \frac{\partial p'}{\partial x}$ and

$$\Delta p \;=\; \Delta p' \;=\; p'_R - p'_L. \tag{122}$$

We denote the relative errors of the approximations $\widetilde{p'_L}$ of p'_L and $\widetilde{p'_R}$ of p'_R by ϵ'_L and ϵ'_R, respectively, i.e.

$$\widetilde{p'_L} \;=\; p'_L(1+\epsilon'_L), \qquad \widetilde{p'_R} \;=\; p'_R(1+\epsilon'_R). \tag{123}$$

Thus, we get

$$\widetilde{\Delta p'} \;=\; \widetilde{p'_R} - \widetilde{p'_L} \;=\; \Delta p(1 + \frac{p'_R}{\Delta p}\epsilon'_R - \frac{p'_L}{\Delta p}\epsilon'_L). \tag{124}$$

Since $p'_L = p_L - p_0$ and $p'_R = p_R - p_0$ are of the order $O(M)$ and $O(M^2)$ for unsteady and steady flow, respectively, the condition numbers $\frac{p'_L}{\Delta p}$ and $\frac{p'_R}{\Delta p}$ are indeed of order $O(1)$, as claimed above. Thus, cancellation of the pressure difference can be avoided by using the perturbed pressure (121).

In order to avoid cancellation also for other terms and in order to retain the conservative form of the Navier-Stokes equations, we introduce the perturbed conservative variables

$$\mathbf{U}'(\mathbf{x},t) \;=\; \mathbf{U}(\mathbf{x},t) - \mathbf{U}_0, \tag{125}$$

where $\mathbf{U}' = (\rho', (\rho\mathbf{u})', (\rho E)')^T$ and $\mathbf{U}_0 = (1, 0, \frac{1}{\gamma-1})^T$, if we choose the stagnation conditions as the reference quantities in the nondimensionalization (13). Using the dependence

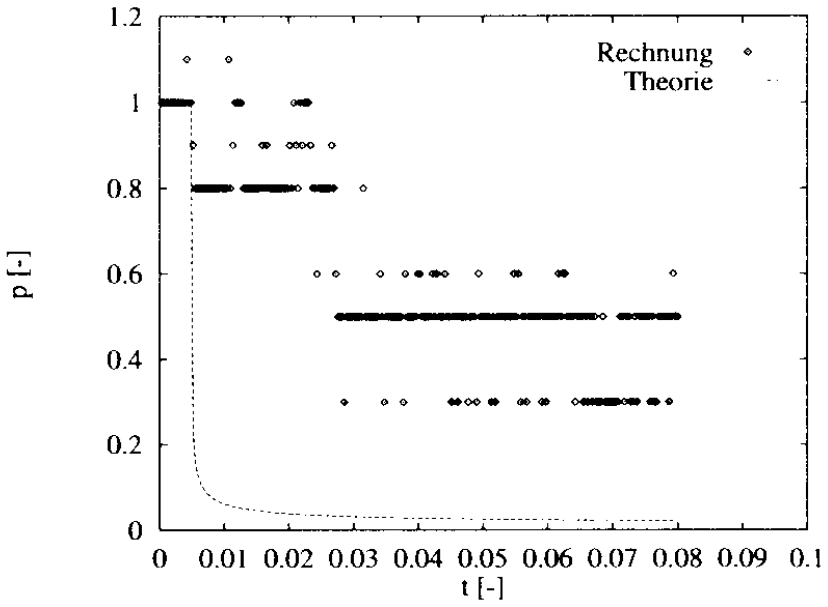

Figure 13: Pressure at an x location for $M = 10^{-6}$, $\diamond$: computed result with conservative formulation and single precision, $\cdots$: analytical solution.

of velocity, pressure and total enthalpy on the conservative variables, we get the following relations

$$\mathbf{u}' = \frac{(\rho\mathbf{u})'}{\rho_0 + \rho'}, \tag{126}$$

$$p' = (\gamma - 1)[(\rho E)' - \tilde{M}^2 \frac{1}{2}(\rho\mathbf{u})' \cdot \mathbf{u}'], \tag{127}$$

$$(\rho H)' = (\rho E)' + p'. \tag{128}$$

We reformulate the Navier-Stokes equations in terms of the perturbed conservative variables as

$$\frac{\partial \rho'}{\partial t} + \boldsymbol{\nabla} \cdot (\rho\mathbf{u})' = 0 \tag{129}$$

$$\frac{\partial (\rho\mathbf{u})'}{\partial t} + \boldsymbol{\nabla} \cdot (\rho\mathbf{u})'\mathbf{u}' + \frac{1}{\tilde{M}^2}\boldsymbol{\nabla} p' = \mathbf{G}' \tag{130}$$

$$\frac{\partial (\rho E)'}{\partial t} + \boldsymbol{\nabla} \cdot ((\rho H)'\mathbf{u}' + (\rho H)_0\mathbf{u}') = Q' \tag{131}$$

where $\mathbf{G}' = \frac{1}{Re_\infty}\boldsymbol{\nabla} \cdot \boldsymbol{\tau}' + \frac{1}{Fr_\infty^2}\rho'(-\mathbf{e}_r)$ with $\boldsymbol{\tau}' = \mu(\boldsymbol{\nabla}\mathbf{u}' + (\boldsymbol{\nabla}\mathbf{u}')^T) - \frac{2}{3}\mu\boldsymbol{\nabla} \cdot \mathbf{u}'\,\mathbf{I}$.

$Q' = \frac{\tilde{M}^2}{Re_\infty}\boldsymbol{\nabla} \cdot (\boldsymbol{\tau}' \cdot \mathbf{u}') + \frac{\tilde{M}^2}{Fr_\infty^2}(\rho\mathbf{u})' \cdot (-\mathbf{e}_r) + \frac{\gamma}{(\gamma-1)Re_\infty Pr_\infty}\boldsymbol{\nabla} \cdot (\kappa\boldsymbol{\nabla}T') + \rho' q_0 + (\rho_0 + \rho')q'$

with $T' = (p' - \rho' T_0)/(\rho_0 + \rho')$, $\mu = \mu(T_0 + T')$, $\kappa = \mu$ for $Pr = Pr_\infty$, $q' = q - q(\mathbf{U}_0)$.

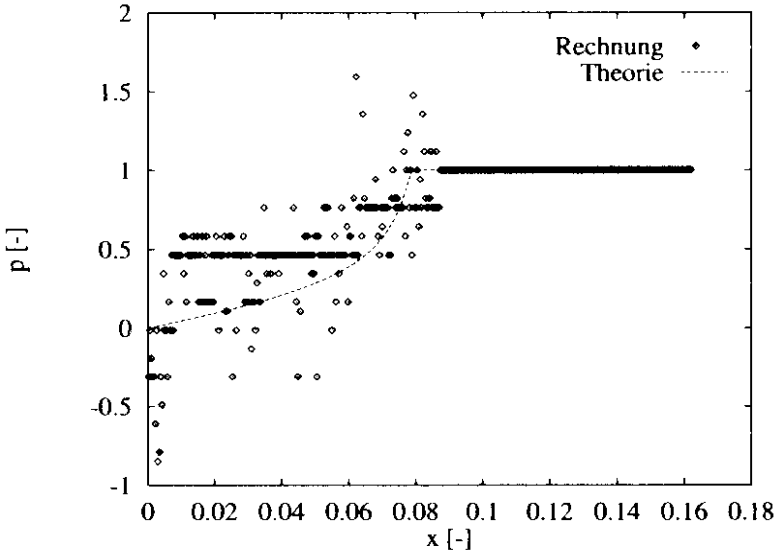

Figure 14: Pressure at a time instant for $M = 10^{-6}$, $\diamond$: computed result with conservative formulation and single precision, $\cdots$: analytical solution.

The present perturbation formulation does not neglect anything, neither a linear nor a nonlinear term: the Navier-Stokes equations in perturbation form (129), (130), (131) are analytically equal to the Navier-Stokes equations in conservative form (16), (17), (18). However, the discretization of $\frac{\partial \rho'}{\partial t}$, $\boldsymbol{\nabla} p'$ and $\frac{\partial (\rho E)'}{\partial t}$ is well-conditioned opposed to $\frac{\partial \rho}{\partial t}$, $\boldsymbol{\nabla} p$ and $\frac{\partial (\rho E)}{\partial t}$.

In the energy equation (131), we should discretize $\boldsymbol{\nabla} \cdot (\rho H)_0 \mathbf{u}'$ as $(\rho H)_0 \boldsymbol{\nabla} \cdot \mathbf{u}'$, of course, to avoid cancellation there. The shear stress tensors $\boldsymbol{\tau}'$ and $\boldsymbol{\tau}$ are equal, because $\mathbf{u}'$ and $\mathbf{u}$ are equal. Discretizing $\boldsymbol{\nabla} T'$ in (131) instead of $\boldsymbol{\nabla} T$ in (18) avoids cancellation in the heat conduction.

Central discretizations of the Navier-Stokes equations in perturbation form are as straightforward as for the conservative form. For non-central discretizations of scalar derivatives, there is no essential difference either, e.g. the same one-sided finite difference stencil for discretizing $\frac{\partial p}{\partial x}$ at a boundary can be used for $\frac{\partial p'}{\partial x}$. Of course, also the initial and boundary conditions have to be formulated in perturbation form.

However, if a discretization employs information based on a system of equations, e.g. a Riemann solver for the Euler equations, we must be a little bit more careful with the perturbation formulation. For example, if we need the speed of sound, we cannot simply use $\sqrt{\gamma p'/\rho'}$ but have to calculate $c = \sqrt{\gamma (p_0 + p')/(\rho_0 + \rho')}$ correctly, of course. In the next section, we shall see an example how to use an approximate Riemann solver for the Euler equations with the perturbation formulation.

2.5 Characteristic Based Approximate Riemann Solver

First, we illustrate a characteristic based approximate Riemann solver for the 2D Euler equations in conservative form [121], [98]. Then, we show its application in perturbation form [98], [116].

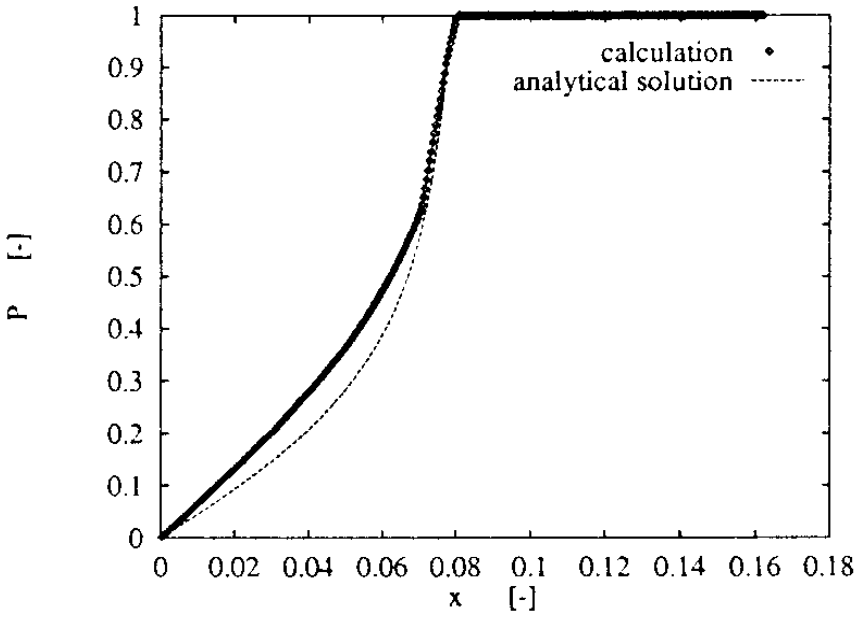

Figure 15: Pressure at a time instant for $M = 10^{-2}$, $\diamond$: computed result with conservative formulation and single precision, dashed line: analytical solution.

Let us consider the evaluation of the flux

$$\mathbf{F}(\mathbf{U}) = \begin{pmatrix} \rho u \\ \rho u^2 + \frac{1}{\tilde{M}^2} p \\ \rho u v \\ \rho H u \end{pmatrix}, \tag{132}$$

where $\mathbf{U} = (\rho, \rho u, \rho v, \rho E)^T$, at a cell interface $x_{i-1/2} = 0$ using the cell-centered finite volume approach. Neglecting multidimensional effects, we define the Riemann problem

$$\frac{\partial \mathbf{U}}{\partial t} + \frac{\partial \mathbf{F}(\mathbf{U})}{\partial x} = 0 \quad , \quad -\infty < x < \infty \ , \ t > 0, \tag{133}$$

$$\mathbf{U}(x, t = 0) = \begin{cases} \mathbf{U}_A & for \quad x < 0 \\ \mathbf{U}_B & for \quad x > 0 \end{cases} \tag{134}$$

As the left and right states, we choose for a first-order method $\mathbf{U}_A = \mathbf{U}_{i-1}^n$ and $\mathbf{U}_B = \mathbf{U}_i^n$, i.e. the cell averages in the left cell $i-1$ and the right cell i at the already calculated time level n. For higher order, we may use the MUSCL or ENO approach.

The Jacobian matrix $\mathbf{A} = \frac{\partial \mathbf{F}}{\partial \mathbf{U}}$ of the flux $\mathbf{F}$ can be diagonalized

$$\mathbf{A} = \mathbf{R} \mathbf{\Lambda} \mathbf{R}^{-1}, \tag{135}$$

where the diagonal matrix $\mathbf{\Lambda} = diag(u - c/\tilde{M}, u, u, u + c/\tilde{M})$ contains the eigenvalues of $\mathbf{A}$. Note that $c = \sqrt{\frac{\gamma p^*/p_\infty^*}{\rho^*/\rho_\infty^*}}$. The 4×4 matrices $\mathbf{R}$ and $\mathbf{R}^{-1}$ contain the right and left eigenvectors of $\mathbf{A}$, respectively [50]. Using the chain rule, we write equation (133) in a non-conservative form

$$\frac{\partial \mathbf{U}}{\partial t} + \mathbf{A} \frac{\partial \mathbf{U}}{\partial x} = 0. \tag{136}$$

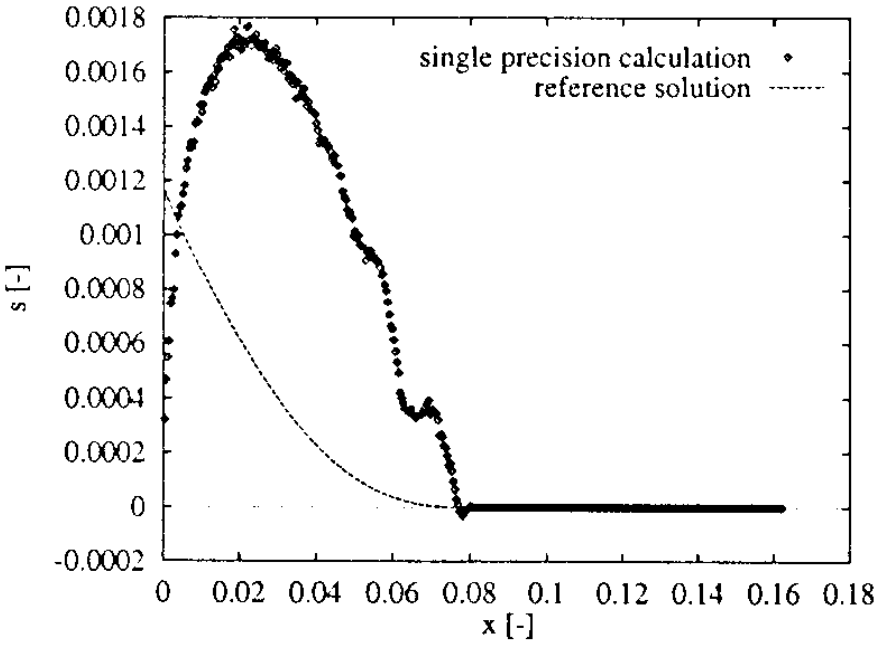

Figure 16: Entropy along the axis of the tube at a time instant for $M = 10^{-2}$, $\diamond$: computed result with conservative formulation and single precision, dashed line: reference solution with double precision.

Multiplying (136) with $\mathbf{R}^{-1}$ from the left hand side and using (135), we obtain the characteristic relations

$$\frac{\partial \mathbf{W}}{\partial t} + \mathbf{\Lambda}\frac{\partial \mathbf{W}}{\partial x} = 0, \tag{137}$$

where $\partial \mathbf{W} = \mathbf{R}^{-1}\partial \mathbf{U} = \begin{pmatrix} \partial p - \tilde{M}\rho c \partial u \\ \partial p - c^2 \partial \rho \\ \partial v \\ \partial p + \tilde{M}\rho c \partial u \end{pmatrix}$.

Thus, on the characteristics (Fig. 18), we obtain the system of ODEs

$$dp - \tilde{M}\rho c\, du = 0 \quad on \quad \frac{dx}{dt} = u - c/\tilde{M}, \tag{138}$$

$$dp - c^2\, d\rho = 0 \quad on \quad \frac{dx}{dt} = u, \tag{139}$$

$$dv = 0 \quad on \quad \frac{dx}{dt} = u, \tag{140}$$

$$dp + \tilde{M}\rho c\, du = 0 \quad on \quad \frac{dx}{dt} = u + c/\tilde{M}. \tag{141}$$

The dimensional form of characteristic equations (138) - (141) reads

$$dp^* - \rho^* c^*\, du^* = 0 \quad on \quad \frac{dx^*}{dt^*} = u^* - c^*, \tag{142}$$

$$dp^* - (c^*)^2\, d\rho^* = 0 \quad on \quad \frac{dx^*}{dt^*} = u^*, \tag{143}$$

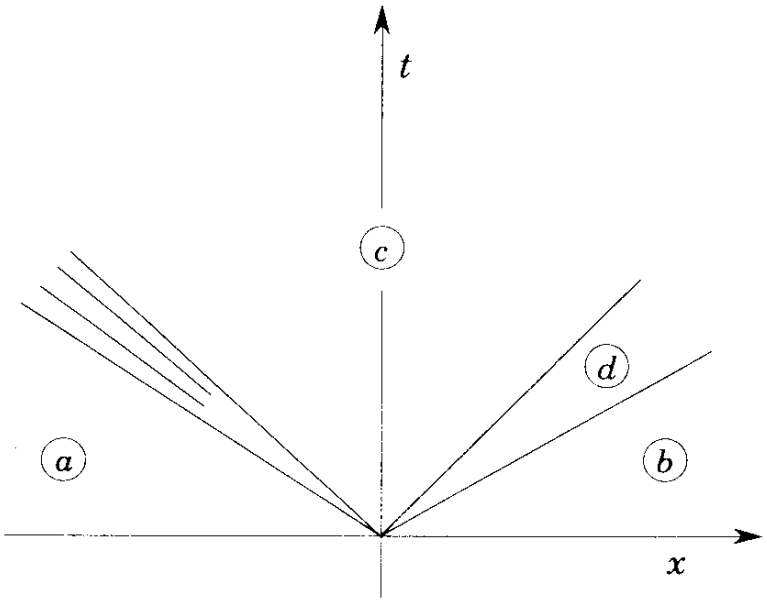

Figure 17: Typical wave pattern of the solution to the Riemann problem.

$$dv^* = 0 \quad on \quad \frac{dx^*}{dt^*} = u^*, \tag{144}$$

$$dp^* + \rho^* c^*\, du^* = 0 \quad on \quad \frac{dx^*}{dt^*} = u^* + c^*. \tag{145}$$

A typical wave pattern of the solution of the Riemann problem (134) is sketched in Fig. (Fig. 17). To solve the Riemann problem (134) approximately, we assume that the characteristic equations of the acoustic waves (138) and (141) even hold across shocks. Since we consider low Mach number flow, that assumption is reasonable. Because $dp = 0$ and $du = 0$ across contact discontinuities, the characteristic equations (138) and (141) are valid across contact discontinuities. In order to determine the flow at the cell interface at the time Δt (or rather $\Delta t/2$ to get $O(\Delta t^2)$ cheaply), we first linearize the acoustic relations (138) and (141) as in the method of characteristics. We denote the flow state, which we want to determine by C, cf. Fig. 19, and obtain

$$p_C - p_B - \tilde{M}\rho_B c_B(u_C - u_B) = 0, \tag{146}$$

$$p_C - p_A + \tilde{M}\rho_A c_A(u_C - u_A) = 0. \tag{147}$$

Since the x-velocity and pressure in regions A and B are known, equations (146) and (147) define the linear system

$$\mathcal{A}\,\alpha = \beta, \tag{148}$$

where

$$\mathcal{A} = \begin{pmatrix} 1 & -\tilde{M}\rho_B c_B \\ 1 & \tilde{M}\rho_A c_A \end{pmatrix}, \qquad \beta = \begin{pmatrix} p_B - \tilde{M}\rho_B c_B u_B \\ p_A + \tilde{M}\rho_A c_A u_A \end{pmatrix}$$

for $\alpha = (p_C, u_C)^T$.

For $\tilde{M} \neq 0$, the matrix $\mathcal{A}$ is non-singular, because the determinant of $\mathcal{A}$ is non-zero.

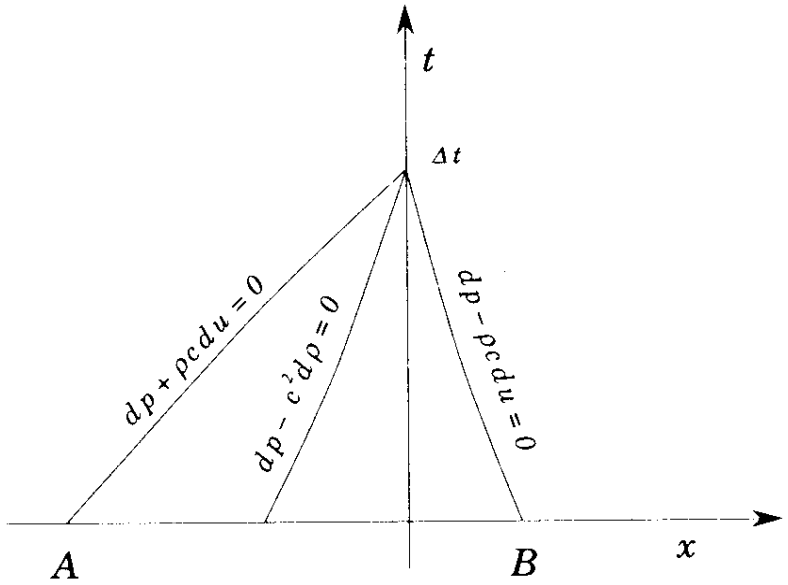

Figure 18: Characteristics and characteristic relations.

Since ρc is of the order $O(1)$ for low Mach number flow, the condition number of $\mathcal{A}$ $cond(\mathcal{A}) = \|\mathcal{A}\| \, \|\mathcal{A}^{-1}\|$ is of the order $O(\tilde{M}^{-1})$. That means that the linear system (148) is ill-conditioned for $\tilde{M} \longrightarrow 0$. However, if we define (146) and (147) as a linear system for $\tilde{\alpha} = (p_C, \tilde{M} u_C)^T$, it is well-conditioned for low Mach numbers, because the condition number of the corresponding matrix $\tilde{\mathcal{A}} = \begin{pmatrix} 1 & -\rho_B c_B \\ 1 & \rho_A c_A \end{pmatrix}$ is of the order $O(1)$.

That finding suggests to nondimensionalize the velocity as

$$\hat{u} = \frac{u^*}{\sqrt{p^*_\infty / \rho^*_\infty}} = \tilde{M} u \tag{149}$$

instead of $u = \frac{u^*}{u^*_\infty}$.

If $u_C = 0$, the flux is simply $\mathbf{F}_C = (0, p_C, 0, 0)^T$. If $u_C > 0$ ($u_C < 0$), the entropy and vorticity waves are convected from A to the right (from B to the left, respectively). Thus, we choose the state A to linearize the linear waves (139), (140), if $u_C > 0$ (B, if $u_C < 0$). Let us assume that $u_C > 0$. Then, we get

$$p_C - p_A - (c_A)^2(\rho_C - \rho_A) = 0, \tag{150}$$

$$v_C - v_A = 0. \tag{151}$$

Thus, ρ_C and v_C can be easily determined from (150) and (151), respectively.

In the perturbation formulation, the characteristic relations (138) - (141) become

$$dp' - \tilde{M} \rho c \, du' = 0 \quad on \quad \frac{dx}{dt} = u' - c/\tilde{M}, \tag{152}$$

$$dp' - c^2 \, d\rho' = 0 \quad on \quad \frac{dx}{dt} = u', \tag{153}$$

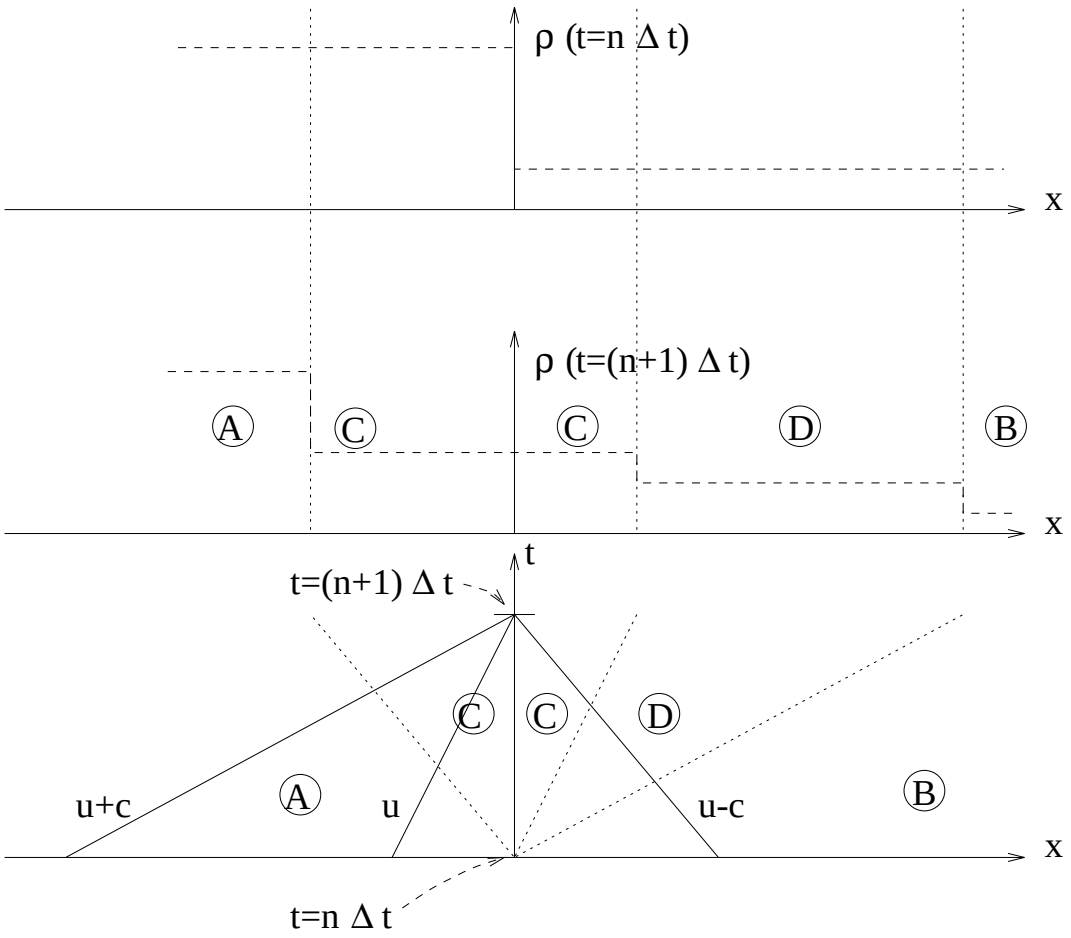

Figure 19: Characteristic based Riemann solver.

$$dv' = 0 \quad on \quad \frac{dx}{dt} = u', \tag{154}$$

$$dp' + \tilde{M}\rho c\, du' = 0 \quad on \quad \frac{dx}{dt} = u' + c/\tilde{M}. \tag{155}$$

Assuming again $u_C > 0$ and using $u'_C = u_C$, the linearization of (152) - (155) yields

$$p'_C - p'_B - \tilde{M}\rho_B c_B(u'_C - u'_B) = 0, \tag{156}$$

$$p'_C - p'_A - (c_A)^2(\rho'_C - \rho'_A) = 0, \tag{157}$$

$$v'_C - v'_A = 0, \tag{158}$$

$$p'_C - p'_A + \tilde{M}\rho_A c_A(u'_C - u'_A) = 0. \tag{159}$$

There is no cancellation problem in computing the expressions $\rho c = \sqrt{\gamma p \rho}$ and $c^2 = \gamma p/\rho$ using $p = p_0 + p'$ and $\rho = \rho_0 + p'$. Equations (156) and (159) determine p'_C and $\tilde{M}u'_C$ without cancellation problem. (157) and (158) yield ρ'_C and v'_C.
Knowing ρ'_C, u'_C, v'_C and p'_C, we can compute the perturbed flux at the cell interface, i.e.

$$\mathbf{F}'(\mathbf{U}_0, \mathbf{U}') = \begin{pmatrix} (\rho u)' \\ (\rho u)'u' + \frac{1}{\tilde{M}^2}p' \\ (\rho u)'v' \\ (\rho H)'u' + (\rho H)_0 u' \end{pmatrix}. \tag{160}$$

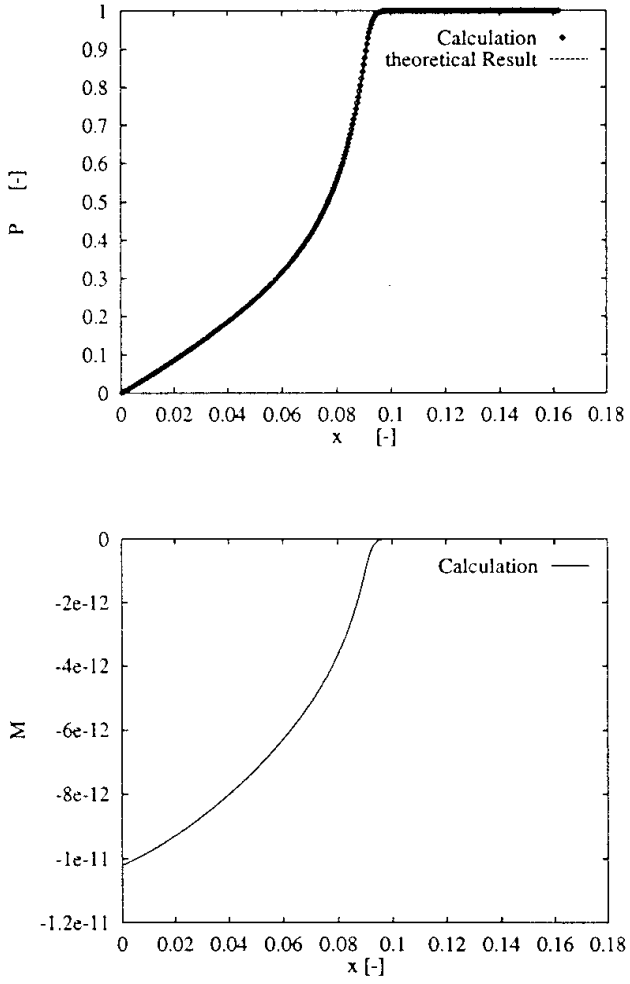

Figure 20: Pressure and Mach number at a time instant for $M = 10^{-11}$, $\diamond$ and solid line: computed result with perturbation formulation and single precision, dashed line: analytical solution.

Thus, we can also avoid cancellation in the computation of the flux.

If we use the perturbation formulation to avoid cancellation in $\frac{\partial \rho}{\partial t}$, $\boldsymbol{\nabla} p$, $\frac{\partial (\rho E)}{\partial t}$ and the flux evaluation, we can avoid the cancellation error in low Mach number computations. Using that approach, Sesterhenn was able to calculate an expansion wave in the long thin tube (Fig. 11) for an outflow Mach number of $M = 10^{-11}$ correctly [98], [116]. Fig. 20 shows the pressure and Mach number computed with the perturbation formulation using single precision and 400×8 cells.

For steady low Mach number flow simulations, Sesterhenn obtained a significant convergence improvement when using a multigrid method with the perturbation formulation instead of the conventional conservative formulation [98]. The error modes introduced by cancellation with the conventional formulation are absent in the perturbation formulation.

3 Conclusions

3.1 Asymptotic Analysis

A single time and space scale asymptotic analysis of the compressible Navier-Stokes equations is shown to lead to the low Mach number equations in the zero Mach number limit. The low Mach number equations allow for large density and temperature variations, for example in combustion. The pressure is split into the sum of the large global thermodynamic pressure and the very small 'incompressible' pressure. The global thermodynamic pressure is constant in space and may only vary in time due to nonzero volume flow and nonzero net heat conduction and heat release rate in the domain of interest. The 'incompressible' pressure only appears in the momentum equation and is determined in a similar way as in incompressible flow. However, the velocity divergence is in general not zero but depends on heat conduction and heat release rate as well as the time change of the global thermodynamic pressure. Since density and temperature are related by the equation of state to the global thermodynamic pressure, any variation of the very small 'incompressible' pressure does not affect density and temperature. Therefore, acoustics is removed from the low Mach number equations.

A multiple time scale, single space scale asymptotic analysis of the compressible Navier-Stokes equations at low Mach numbers splits the pressure into the sum of the large global thermodynamic pressure, the small acoustic pressure and the very small 'incompressible' pressure. The analysis reveals in which way the heat release rate and heat conduction affect the global thermodynamic pressure, the divergence of velocity and the material change of density at low Mach numbers. The asymptotic analysis identifies the acoustic time change of the heat release rate as the dominant source of sound in low Mach number flow. The sound generation and propagation are governed by an inhomogeneous wave equation for the acoustic pressure. If the flow equations are averaged over an acoustic wave period, the averaged velocity tensor describes the net acoustic effect on the averaged flow field. Removing acoustics from the equations altogether leads again to the low Mach number equations.

3.2 Numerical Implications

The low Mach number asymptotics provides a guidance for the choice of the equations. If we are not interested in acoustic effects in low speed combustion for example, we can use the low Mach number equations to avoid the numerical trouble caused by the fast acoustic waves. If the compressible Euler or Navier-Stokes equations are solved at low Mach number, the large disparity of flow velocity and speed of sound introduces a stiffness, which is absent in incompressible flow. The stiffness can be removed by proper time derivative preconditioning for steady flow. For unsteady flow, semi-implicit methods can treat the stiff and non-stiff terms appropriately. The large length scale disparity in low Mach number aeroacoustics calls for fine grids and highly accurate numerical methods. Non-reflecting boundary conditions at artificial boundaries are decisive for the accuracy and convergence of unsteady and steady low Mach number flow simulations, respectively.

Since the discretization of the small changes of the thermodynamic variables like the pressure in low Mach number flow is ill-conditioned, it leads to cancellation errors. The cancellation problem can be avoided by discretizing the perturbation form of the Navier-Stokes equations. The changes of the conservative variables with respect to stagnation conditions are considered as the unknowns. Since the stagnation state is assumed to be

constant in space and time, the resulting perturbation equations are not much different from the conventional conservative form. As the discretization of the perturbation form is well-conditioned, cancellation errors are avoided. A characteristic based approximate Riemann solver is introduced. It yields a simple flux evaluation with the finite volume method and is well suited for low Mach number flows with discontinuities. The implementation of the perturbation form is detailed for the flux evaluation with the characteristic based approximate Riemann solver. Using the perturbation form, even very low Mach number flow problems can be accurately solved with single precision.

Acknowledgements

The author acknowledges the contributions to part 2 by Dr. J. Sesterhenn and Prof. H. Thomann, Institute of Fluid Dynamics, ETH Zürich. Most of the author's research presented in these lecture notes was performed at the Institute of Fluid Dynamics, ETH Zürich. Part of the research for part 1 was done during a stay with Prof. P.J. Zandbergen's group at the Faculty of Applied Mathematics, University of Twente. Since 1998, the present research has been supported by TFR, the Swedish Research Council for Engineering Sciences, under the author's project title "Numerical Simulation of Vortex Sound". The inspiring atmosphere at the Department of Scientific Computing, Uppsala University, is gratefully acknowledged.

References

[1] J. Lighthill. *A General Introduction to Aeroacoustics and Atmospheric Sound*, pages 3–40. Computational Aeroacoustics. Springer-Verlag, New York, 1993. Edited by J.C. Hardin and M.Y. Hussaini.

[2] D.G. Crighton. *Computational Aeroacoustics for Low Mach Number Flows*, pages 50–68. Computational Aeroacoustics. Springer-Verlag, New York, 1993. Edited by J.C. Hardin and M.Y. Hussaini.

[3] G. Volpe. Performance of compressible flow codes at low Mach numbers. *AIAA Journal*, 31:49–56, 1993.

[4] S. Klainerman and A. Majda. Compressible and incompressible fluids. *Communications on Pure and Applied Mathematics*, 35:629–651, 1982.

[5] H.-O. Kreiss, J. Lorenz, and M.J. Naughton. Convergence of the solutions of the compressible to the solutions of the incompressible Navier-Stokes equations. *Advances in Applied Mathematics*, 12:187–214, 1991.

[6] A. Majda. *Compressible Fluid Flow and Systems of Conservation Laws in Several Space Variables*. Springer-Verlag, New York, 1984.

[7] J.K. Hunter, A. Majda, and R. Rosales. Resonantly interacting, weakly nonlinear hyperbolic waves. II. Several space variables. *Studies in Applied Mathematics*, 75:187–226, 1986.

[8] A. Majda, R. Rosales, and M. Schonbek. A canonical system of integrodifferential equations arising in resonant nonlinear acoustics. *Studies in Applied Mathematics*, 79:205–262, 1988.

[9] R.F. Almgren. High-frequency acoustic waves in a reacting gas. *SIAM Journal of Applied Mathematics*, 51:351–373, 1991.

[10] R.G. Rehm and H.R. Baum. The equations of motion for thermally driven buoyant flows. *Journal of Research of the National Bureau of Standards*, 83:297–308, 1978.

[11] Fedorchenko A.T. A model of unsteady subsonic flow with acoustics excluded. *Journal of Fluid Mechanics*, 334:135–155, 1997.

[12] G.P. Zank and W.H. Matthaeus. The equations of nearly incompressible fluids. I. Hydrodynamics, turbulence, and waves. *The Physics of Fluids A*, 3:69–82, 1991.

[13] R. Klein. Semi-implicit extension of a Godunov-type scheme based on low Mach number asymptotics I: One-dimensional flow. *Journal of Computational Physics*, 121:213–237, 1995.

[14] B. Müller. Computation of compressible low Mach number flow. Habilitation thesis, ETH Zürich, 1996.

[15] B. Müller. Low Mach number asyptotics of the Navier-Stokes equations. *Journal of Engineering Mathematics*, 34:97–109, 1998.

[16] J.R. Ristorcelli. A closure for the compressibility of the source terms in Lighthill's acoustic analogy. ICASE Report No. 97-44, 1997.

[17] A. Majda and J. Sethian. The derivation and numerical solution of the equations for zero Mach number combustion. *Combustion Science and Technology*, 42:185–205, 1985.

[18] H.-O. Kreiss and J. Lorenz. *Initial-Boundary Value Problems and the Navier-Stokes Equations*. Academic Press, New York, 1989.

[19] W. Schneider. *Mathematische Methoden der Strömungsmechanik*. Vieweg, Braunschweig, 1978.

[20] A.H. Nayfeh. *Introduction to Perturbation Techniques*. John Wiley & Sons, New York, 1981.

[21] H.A. Dwyer. Calculation of low Mach number reacting flows. *AIAA Journal*, 28:98–105, 1990.

[22] J.J. Keller. Thermoacoustic oscillations in combustion chambers of gas turbines. *AIAA Journal*, 33:2280–2287, 1995.

[23] G.H. Schneider. *Kompression und Expansion eines Gases in einem Zylinder als Störungsproblem*. PhD thesis, TU Wien, 1977.

[24] R. Klein and N. Peters. Cumulative effects of weak pressure waves during the induction period of a thermal explosion in a closed cylinder. *Journal of Fluid Mechanics*, 187:197–230, 1988.

[25] R.H. Rhadwan and D.R. Kassoy. The response of a confined gas to a thermal disturbance: Rapid boundary heating. *Journal of Engineering Mathematics*, 18:133–156, 1984.

[26] J. Kevorkian and J.D. Cole. *Multiple Scale and Singular Perturbation Methods.* Springer-Verlag, New York, 1996.

[27] A.P. Dowling. *Thermoacoustic Sources and Instabilities*, pages 378–405. Modern Methods in Analytical Acoustics. Springer-Verlag, London, 1992. Lecture Notes by D.G. Crighton and A.P. Dowling and J.E. Ffowcs Williams and M. Heckl and F.G. Leppington.

[28] P. Clavin. Premixed combustion and gasdynamics. *Annual Review of Fluid Mechanics*, 26:321–352, 1994.

[29] J. Lighthill. On sound generated aerodynamically. I. General theory. *Proceedings of the Royal Society of London A*, 211:564–587, 1952.

[30] H.-O. Kreiss. *Problems with Different Time Scales and Acoustics*, pages 156–166. Computational Aeroacoustics. Springer-Verlag, New York, 1993. Edited by J.C. Hardin and M.Y. Hussaini.

[31] A.P. Dowling and J.E. Ffowcs Williams. *Sound and Sources of Sound.* Ellis Horwood Limited, Chichester, 1983.

[32] M. Roger. Fundamentals of aero-acoustics. Applied Aero-Acoustics: Prediction Methods, VKI Lecture Series 1996-04, 1996.

[33] V.L. Wells and R.A. Renaut. Computing aerodynamically generated noise. *Annual Review of Fluid Mechanics*, 29:161–199, 1997.

[34] A.S. Lyrintzis. Review: The use of Kirchhoff's method in computational aeroacoustics. *Journal of Fluids Engineering*, 116:665–676, 1994.

[35] C.K.W. Tam. Computational aeroacoustics: Issues and methods. *AIAA Journal*, 33:1788–1796, 1995.

[36] M. Hardin. Computational approaches to aeroacoustics. Applied Aero-Acoustics: Prediction Methods, VKI Lecture Series 1996-04, 1996.

[37] H. Reister. *Numerische Simulation der Wechselwirkung von Druckwellen mit laminaren und turbulenten Grenzschichten.* PhD thesis, Universität Karlsruhe and DFVLR-FB 87-18, 1987.

[38] C.J. Moore. The role of shear-layer instability waves in jet exhaust noise. *Journal of Fluid Mechanics*, 80:321–367, 1977.

[39] B. Gustafsson, H.-O. Kreiss, and J. Oliger. *Time Dependent Problems and Difference Methods.* John Wiley & Sons, New York, 1995.

[40] S. K. Lele. Compact finite difference schemes with spectral-like resolution. *Journal of Computational Physics*, 103:16–42, 1992.

[41] W. Möhring. On vortex sound at low Mach number. *Journal of Fluid Mechanics*, 85:685–691, 1978.

[42] W. Möhring. *Modelling Low Mach Number Noise*, pages 85–96. Mechanics of Sound Generation in Flows. Springer-Verlag, Berlin, 1979. Edited by E.-A. Müller.

[43] B. Engquist and A. Majda. Absorbing boundary conditions for the numerical simulation of waves. *Mathematics of Computation*, 31:629–651, 1977.

[44] M.B Giles. Nonreflecting boundary conditions for Euler equation calculations. *AIAA Journal*, 28:2050–2058, 1990.

[45] D. Kröner. Absorbing boundary conditions for the linearized Euler equations in 2-D. *Mathematics of Computation*, 57:153–167, 1991.

[46] A.P. Saxer and M.B Giles. Quasi-three-dimensional nonreflecting boundary conditions for Euler equations calculations. *Journal of Propulsion and Power*, 9:263–271, 1993.

[47] L. Ferm and B. Gustafsson. A down-stream boundary procedure for the Euler equations. *Computers Fluids*, 10:261–276, 1982.

[48] L. Ferm. Non-reflecting boundary conditions for the steady Euler equations. *Journal of Computational Physics*, 122:307–316, 1995.

[49] A. Verhoff. Modeling of computational and solid surface boundary conditions for fluid dynamics calculations. AIAA Paper 85-1496-CP, 1985.

[50] C. Hirsch. *Numerical Computation of Internal and External Flows*. John Wiley & Sons, Chichester, 1990. Volume 2.

[51] K.W. Thompson. Time dependent boundary conditions for hyperbolic systems. *Journal of Computational Physics*, 68:1–24, 1987.

[52] K.W. Thompson. Time-dependent boundary conditions for hyperbolic systems, II. *Journal of Computational Physics*, 89:439–461, 1990.

[53] A. Bayliss and E. Turkel. Far field boundary conditions for compressible flows. *Journal of Computational Physics*, 48:182–199, 1982.

[54] C.K.W. Tam and J.C. Webb. Dispersion-relation-preserving finite difference schemes for computational acoustics. *Journal of Computational Physics*, 107:262–281, 1993.

[55] B. Müller. *Influence of Inlet and Outlet Boundary Conditions in Internal Flow Computations at Low Mach Numbers*, pages 637–643. 3rd ECCOMAS CFD Conference, Paris, 9-13 Sept. 1996. John Wiley & Sons, Chichester, 1996. Edited by J.-A. Désidéri, C. Hirsch, P. LeTallec, M. Pandolfi, and J. Périaux.

[56] B. Gustafsson and A. Sundström. Incompletely parabolic problems in fluid dynamics. *SIAM Journal on Applied Mathematics*, 35:343–357, 1978.

[57] L. Halpern. Artificial boundary conditions for incompletely parabolic perturbations of hyperbolic systems. *SIAM Journal on Mathematical Analysis*, 22:1256–1283, 1991.

[58] G. Lill. Exact and approximate boundary conditions at artificial boundaries. Preprint Nr. 1478, FB Mathematik, TH Darmstadt, 1992.

[59] J. Nordström. The use of characteristic boundary conditions for the Navier-Stokes equations. *Computers Fluids*, 24:609–623, 1995.

[60] T.J. Poinsot and S.K. Lele. Boundary conditions for direct simulations of compressible viscous flows. *Journal of Computational Physics*, 101:104–129, 1992.

[61] T. Colonius, S.K. Lele, and P. Moin. Boundary conditions for direct computation of aerodynamic sound generation. *AIAA Journal*, 31:1574–1582, 1993.

[62] M. Baum, T.J. Poinsot, and D. Thévenin. Accurate boundary conditions for multicomponent reactive flows. *Journal of Computational Physics*, 116:247–261, 1994.

[63] H. Atkins and J. Casper. Nonreflective boundary conditions for high-order methods. *AIAA Journal*, 32:512–518, 1994.

[64] J. Lighthill. *Waves in Fluids.* Cambridge University Press, Cambridge, 1978.

[65] L.D. Landau and E.M. Lifshitz. *Fluid Mechanics.* Pergamon Press, Oxford, 2nd edition, 1993.

[66] A.D. Pierce. *Acoustics: An Introduction to Its Physical Priciples and Applications.* Acoustical Society of America, Woodbury, 2nd edition, 1991.

[67] R.R. Mankbadi. *Transition, Turbulence, and Noise: Theory and Applications for Scientists and Engineers.* Kluwer Academic Publishers, Boston, 1994.

[68] J.C. Hardin and M.Y. Hussaini, editors. *Computational Aeroacoustics*, New York, 1993. Springer-Verlag.

[69] S.K. Lele, P. Moin, T. Colonius, and B. Mitchell. *Direct Computations of Aeroacoustic Noise*, pages 325–334. Computational Aeroacoustics. Springer-Verlag, New York, 1993. Edited by J.C. Hardin and M.Y. Hussaini.

[70] Z. Haras and S. Ta'asan. Finite difference schemes for long-time integration. *Journal of Computational Physics*, 114:265–279, 1994.

[71] F.Q. Hu, M.Y. Hussaini, and J.L. Manthey. Low-dissipation and low-dispersion Runge-Kutta schemes for computational acoustics. *Journal of Computational Physics*, 124:177–191, 1996.

[72] J.P. Thomas and P.L. Roe. Development of non-dissipative numerical schemes for computational aeroacoustics. AIAA Paper 93-3382-CP, 1993.

[73] R. Vichnevetsky and J.B. Bowles. *Fourier Analysis of Numerical Approximations of Hyperbolic Equations.* SIAM, Philadelphia, 1982.

[74] M. Streng, H. Kuerten, J. Broeze, and B. Geurts. Parallel algorithms for DNS of compressible flow. In "Progress and Challenges in CFD Methods and Algorithms", AGARD-CP-578, pp. 23-1 to 23-10, 1996.

[75] R.I. Issa. Solution of the implicitly discretized fluid flow equations by operator-splitting. *Journal of Computational Physics*, 62:40–65, 1986.

[76] J.P. Van Doormaal, G.D. Raithby, and B.H. McDonald. The segregated approach to predicting viscous compressible fluid flows. *Transactions of the ASME*, 109:268–277, 1987.

[77] C.M. Rhie. Pressure-based Navier-Stokes solver using the multigrid method. *AIAA Journal*, 27:1017–1018, 1989.

[78] K.C. Karki and S.V. Patankar. Pressure based calculation procedure for viscous flows at all speeds in arbitrary configurations. *AIAA Journal*, 27:1167–1174, 1989.

[79] J.J. McGuirk and G.J. Page. Shock capturing using a pressure-correction method. *AIAA Journal*, 28:1751–1757, 1990.

[80] S.M.H. Kariman and G.E. Schneider. Pressure-based control-volume finite element method for flow at all speeds. *AIAA Journal*, 33:1611–1618, 1995.

[81] M.H. Kobayashi and J.C.F. Pereira. Characteristic-based pressure correction at all speeds. *AIAA Journal*, 34:272–280, 1996.

[82] H. Bijl and P. Wesseling. *A Numerical Method for the Computation of Compressible Flow with Low Mach Number Regions*, pages 206–212. 3rd ECCOMAS CFD Conference, Paris, 9-13 Sept. 1996. John Wiley & Sons, Chichester, 1996. Edited by J.-A. Désidéri, C. Hirsch, P. LeTallec, M. Pandolfi, and J. Périaux.

[83] C.L. Merkle, S. Venkateswaran, and P.E.O. Buelow. The relationship between pressure-based and density-based algorithms. AIAA Paper 92-0425, 1992.

[84] B. van Leer, W.-T. Lee, and P. Roe. Characteristic time-stepping or local preconditioning of the Euler equations. AIAA Paper 91-1552-CP, 1991.

[85] D. Choi and C.L. Merkle. Application of time-iterative schemes to incompressible flow. *AIAA Journal*, 23:1518–1524, 1985.

[86] M.K. Strelets and M.L. Shur. Methods of scaling the compressibility in calculating stationary flows of a viscous gas at arbitrary Mach numbers. *U.S.S.R. Computational Mathematics and Mathematical Physics*, 28:165–173, 1988.

[87] A.G. Godfrey, R.W. Walters, and B. van Leer. Preconditioning for the Navier-Stokes equations with finite-rate chemistry. AIAA Paper 93-0535, 1993.

[88] R. Radespiel, E. Turkel, and N. Kroll. Assessment of preconditioning methods. DLR Forschungsbericht 95-29, 1995.

[89] B. Koren and B. van Leer. Analysis of preconditioning and multigrid for Euler flows with low-subsonic regions. *Advances in Computational Mathematics*, 4:127–144, 1995.

[90] B. Koren. Condition improvement for point relaxation in multigrid, subsonic Euler-flow computations. *Applied Numerical Mathematics*, 16:457–469, 1995.

[91] R.H. Pletcher and K.-H. Chen. On solving the compressible Navier-Stokes equations for unsteady flows at very low Mach numbers. AIAA Paper 93-3368, 1993.

[92] L.-E. Eriksson. *A Preconditioned Navier-Stokes Solver for Low Mach Number Flow*, pages 199–205. 3rd ECCOMAS CFD Conference, Paris, 9-13 September 1996. John Wiley & Sons, Chichester, 1996. Edited by J.-A. Désidéri, C. Hirsch, P. LeTallec, M. Pandolfi, and J. Périaux.

[93] D. Choi and C.L. Merkle. The application of preconditioning in viscous flows. *Journal of Computational Physics*, 105:207–223, 1993.

[94] C.L. Merkle, S. Venkateswaran, and M. Deshpande. Convergence acceleration of the Navier-Stokes equations through time-derivative preconditioning. In "Progress and Challenges in CFD Methods and Algorithms", AGARD-CP-578, 1996.

[95] E. Turkel. Review of preconditioning methods for fluid dynamics. *Applied Numerical Mathematics*, 12:257–284, 1993.

[96] B. Müller, J. Sesterhenn, and H. Thomann. *Preconditioning and Flux Vector Splitting for Compressible Low Mach Number Flow*, pages 125–129. 13th International Conference on Numerical Methods in Fluid Dynamics. Springer-Verlag, Berlin, 1993. Edited by M. Napolitano and F. Sabetta.

[97] J. Sesterhenn, B. Müller, and H. Thomann. Flux-vector splitting for compressible low Mach number flow. *Computers Fluids*, 22:441–451, 1993.

[98] J. Sesterhenn. *Zur numerischen Berechnung kompressibler Strömungen bei kleinen Mach-Zahlen*. PhD thesis, ETH Zürich Nr. 11334, 1995.

[99] K.-H. Chen and R.H. Pletcher. Primitive variable, strongly implicit calculation procedure for viscous flows at all speeds. *AIAA Journal*, 29:1241–1249, 1991.

[100] J. Guerra and B. Gustafsson. A numerical method for incompressible and compressible flow problems with smooth solutions. *Journal of Computational Physics*, 63:377–397, 1986.

[101] B. Gustafsson. Unsymmetric hyperbolic systems and the Euler equations at low Mach numbers. *Journal of Scientific Computing*, 2:123–136, 1987.

[102] B. Gustafsson and H. Stoor. Navier-Stokes equations for almost incompressible flow. *SIAM Journal on Numerical Analysis*, 28:1523–1547, 1991.

[103] V. Casulli and D. Greenspan. Pressure method for the numerical solution of transient, compressible fluid flows. *International Journal for Numerical Methods in Fluids*, 4:1001–1012, 1984.

[104] G. Patnaik, R.H. Guirguis, J.P. Boris, and E.S. Oran. A barely implicit correction for flux-corrected transport. *Journal of Computational Physics*, 71:1–20, 1987.

[105] K.J. Geratz, R. Klein, C.D. Munz, and S. Roller. *Multiple Pressure Variable (MPV) Approach for Low Mach Number Flows Based on Asymptotic Analysis*, pages 340–354. Flow Simulation with High-Performance Computers II. Vieweg, Braunschweig, 1996. Edited by E.H. Hirschel.

[106] O.C. Zienkiewicz, J. Szmelter, and J. Peraire. Compressible and incompressible flow, An algorithm for all seasons. *Computer Methods in Applied Mechanics and Engineering*, 78:105–121, 1990.

[107] O.C. Zienkiewicz and J. Wu. A general explicit or semi-explicit algorithm for compressible and incompressible flows. *International Journal for Numerical Methods in Engineering*, 35:457–479, 1992.

[108] J.P. Collins, P. Colella, and H.M. Glaz. *An Unsplit Implicit-Explicit Godunov Method for Compressible Gas Dynamics*, pages 659–666. 1st ECCOMAS CFD Conference, Brussels, 7-11 Sept. 1992. Elsevier, Amsterdam, 1992. Edited by C. Hirsch, J. Périaux, and W. Kordulla.

[109] G. Erlebacher, M.Y. Hussaini, H.-O. Kreiss, and S. Sarkar. The analysis and simulation of compressible turbulence. *Theoretical and Computational Fluid Dynamics*, 2:73–95, 1990.

[110] S. Abarbanel, P. Duth, and D. Gottlieb. Splitting methods for low Mach number Euler and Navier-Stokes equations. *Computers Fluids*, 17:1–12, 1989.

[111] S.G. Rubin and P.K. Khosla. A review of reduced Navier-Stokes computations for compressible viscous flows. *Computing Systems in Engineering*, 1:549–562, 1990.

[112] M.-S. Liou and C. Steffen. A new flux splitting scheme. *Journal of Computational Physics*, 107:23–39, 1993.

[113] A. Jameson. Artificial diffusion, upwind biasing, limiters and their effect on accuracy and multigrid convergence in transonic and hypersonic flows. AIAA Paper 93-3359, 1993.

[114] C. L. Merkle and Y.-H. Choi. Computation of low-speed flow with heat addition. *AIAA Journal*, 25:831–838, 1987.

[115] A. Dadone and M. Napolitano. A perturbative lambda formulation. *AIAA Journal*, 24:411–417, 1986.

[116] J. Sesterhenn, B. Müller, and H. Thomann. *On the Cancellation Problem in Calculating Compressible Low Mach Number Flows*, pages 408–413. 3rd ECCOMAS CFD Conference, Paris, 9-13 September 1996. John Wiley & Sons, Chichester, 1996. Edited by J.-A. Désidéri, C. Hirsch, P. LeTallec, M. Pandolfi, and J. Périaux.

[117] W.R. Briley, H. McDonald, and S.J. Shamroth. A low Mach number Euler formulation and application to time-iterative LBI schemes. *AIAA Journal*, 21:1467–1469, 1983.

[118] M. Hafez, M. Soliman, and S. White. A unified approach for numerical simulation of viscous compressible and incompressible flows over adiabatic and isothermal walls. "5th Symposium on Numerical and Physical Aspects of Aerodynamic Flows", Long Beach, CA, 1992.

[119] M.T. Heath. *Scientific Computing: An Introductory Survey.* McGraw-Hill, New York, 1997.

[120] F. Aebli and H. Thomann. Stability of the flow behind a pressure pulse in a tube. *Zeitschrift für angewandte Mathematik und Physik*, 39:387–396, 1988.

[121] J. Sesterhenn, B. Müller, and H. Thomann. *A Simple Characteristic Flux Evaluation for Subsonic Flow*, pages 57–61. 2nd ECCOMAS CFD Conference, Stuttgart, 5-8 Sept. 1994. John Wiley & Sons, Chichester, 1994. Edited by S. Wagner, E.H. Hirschel, J. Périaux, and R. Piva.